

NOSE CONE DESIGN OF AN AERIAL DROP VEHICLE

A Major Qualifying Project Report:

submitted to the Faculty

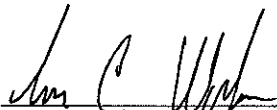
of the

WORCESTER POLYTECHNIC INSTITUTE

in partial fulfillment of the requirements for the

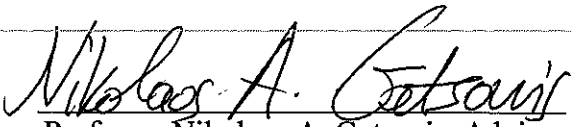
Degree of Bachelor of Science


by


  
\_\_\_\_\_  
Levi C. Wade IV

Date: August 12, 2008

Approved:

  
\_\_\_\_\_  
Professor Nikolaos A. Gatsonis, Advisor  
Mechanical Engineering Department, WPI

  
\_\_\_\_\_  
Professor Mark Richman, Co-Advisor  
Mechanical Engineering Department, WPI

  
\_\_\_\_\_  
Dr. Brian J. Smith, Affiliate Advisor  
KaZaK Composites, Incorporated

---

## Abstract

---

The Sonobuoy Precision Aerial Drop (SPAD) vehicle developed by KaZaK Composites, launched from an aircraft will pilot a sensor package to the ocean surface. This project evaluates a spring-loaded, an inflatable, a rubber, and a foam nose-cone concept for SPAD. Results from aerodynamic analysis of the nose cone are used in structural analysis performed with ANSYS. Fabrication and experimentation with selected concepts supports the analysis. The rubber nose concept conforms with the requirements for structural integrity, weight, functionality, and cost.

**Contract No: N68335-05-C-0422**

**Contractor: KaZaK Composites, Inc**

**Address: 10 F Gill Street, Woburn, MA 01801**

**Expiration Date of SBIR Data Rights: Jan 30, 2014**

The Government's rights to use, modify, reproduce, release, perform, display, or disclose technical data or computer software marked with this legend are restricted during the period shown as provided in paragraph (b)(4) of the Rights in Noncommercial Technical Data and Computer Software—Small Business Innovation Research (SBIR) Program clause contained in the above identified contract. No restrictions apply after the expiration shown above. Any reproduction of technical data, computer software, or portions thereof marked with this legend must also reproduce the markings.

---

## Acknowledgements

---

First, I would like to thank Tony DiCroce, John Schickling and Jerome Fanucci for their assistance in finding a topic for my Major Qualifying Project. Without their help, I would never have been introduced to KaZaK Composites and the SPAD program and for this I am extremely grateful.

I would also like to thank Brian Smith and Stephen Shoenholtz. Their expertise in research and development projects was an excellent guide in keeping me on track throughout the MQP. I thank them for all of their technical assistance and their support.

Last, but certainly not least, I would like to thank Professor Gatsonis. His willingness to advise a summer MQP and his constant patience in all that is an off campus project was all that I could have asked him for and I thank him.

---

# Table of Contents

---

<b>Abstract</b> .....	<b>i</b>
<b>Acknowledgements</b> .....	<b>ii</b>
<b>Table of Contents</b> .....	<b>iii</b>
<b>List of Figures</b> .....	<b>v</b>
<b>List of Equations</b> .....	<b>vii</b>
<b>List of Tables</b> .....	<b>viii</b>
<b>Chapter 1: Introduction</b> .....	<b>1</b>
1.1 Literature Review .....	1
1.2 Project Objectives, Requirements and Approach.....	5
Objectives .....	5
Requirements .....	5
Approach.....	6
<b>Chapter 2: Nose Cone Design</b> .....	<b>9</b>
2.1 Spring-Loaded Nose.....	9
2.1.1 Section One.....	9
2.1.2 Section Two .....	10
2.1.3 Section Three .....	12
2.1.4 Section Four .....	13
2.1.5 Base Plate.....	13
2.1.6 Spring-Loaded Nose Assembly .....	15
2.2 Inflatable Nose .....	17
2.2.1 Inflatable Nose Assembly.....	17
2.2.2 Base Plate.....	18
2.2.3 Inflatable Balloon.....	19
2.2.4 Pressurized Gas Bottle .....	19
2.2.5 Trigger Assembly.....	20
2.3 Rubber Nose.....	21
2.4 Foam Nose.....	22
<b>Chapter 3: Aerodynamic Analysis</b> .....	<b>23</b>
3.1 Methods.....	23
3.2 Procedure.....	25
3.3 Results .....	27
3.3.1 Conformity Analysis.....	27
3.3.2 Maximum Velocity Analysis .....	28
3.3.3 Comparative Analysis.....	31

<b>Chapter 4: Structural Analysis.....</b>	<b>33</b>
4.1 Spring-Loaded Nose.....	34
4.1.1 Mission Mode .....	34
4.1.2 Weight Saving Tradeoff.....	41
4.1.3 Failure Mode.....	46
4.2 Inflatable Nose .....	48
4.3 Rubber Nose.....	49
<b>Chapter 5: Fabrication and Experimentation.....</b>	<b>51</b>
5.1 Fabrication.....	51
5.1.1 Materials and Methods.....	52
5.2 Experimentation .....	55
5.2.1 Foam Nose .....	55
5.2.2 Rubber Nose.....	59
<b>Chapter 6: Summary and Recommendations .....</b>	<b>66</b>
6.1 Spring-Loaded Nose Cone .....	66
6.2 Inflatable Nose .....	67
6.3 Rubber Nose.....	67
6.4 Foam Nose.....	68
6.5 Conclusion.....	68
<b>Acronyms .....</b>	<b>70</b>
<b>Appendix.....</b>	<b>71</b>
Navier-Stokes Equations (Anderson 2007) .....	71
Shear Stress Equations for Fluid Flow (Anderson 2007) .....	72
<b>References .....</b>	<b>73</b>

---

## List of Figures

---

Figure 1-1: SPAD in compressed storage stage.....	4
Figure 1-2: SPAD in extended flight configuration.....	4
Figure 2-1: Spring Loaded Nose, Section One .....	10
Figure 2-2: Spring Loaded Nose, Section Two .....	11
Figure 2-3: Spring-Loaded Nose, Section Three .....	12
Figure 2-4: Spring-Loaded Nose, Section Four .....	13
Figure 2-5: Spring-Loaded Nose, Base Plate Section.....	14
Figure 2-6: Base-Plate to Sonobuoy Wind Flap Connection.....	15
Figure 2-7: Spring-Loaded Nose, Assembly at Full Compression and Total Extension.....	16
Figure 2-8: Inflatable Nose Assembly (Pressure Switch Not Shown).....	18
Figure 2-9: Inflatable Nose Base Plate .....	18
Figure 2-10: Pressurized CO <sub>2</sub> Gas Bottle .....	19
Figure 2-11: Inflatable Nose, Trigger Assembly .....	20
Figure 2-12: Rubber Nose (Wind-Flap Attachment Not Shown).....	21
Figure 2-13: Foam Nose Assembly .....	22
Figure 3-1: GAMBIT Model of the Three-Dimensional SPAD Body with a Hemispherical Nose Cone .....	26
Figure 3-2: SPAD Wind Tunnel Model with Control Surfaces Attached and Deployed in MIT's Wright Brothers Wind Tunnel (Courtesy of KaZaK Composites, Inc.) .....	28
Figure 3-3: CFD Derived Values for SPAD Nose Cone Pressure Distribution @ $\alpha=0^\circ$ , $V_\infty=110$ mph .....	29
Figure 3-4: Pressure Distribution about the SPAD Body @ $\alpha=0^\circ$ , $V_\infty=110$ mph .....	30
Figure 3-5: Velocity Magnitude Profile Across the y-Direction from the SPAD Surface Outward in the Vicinity of the Pitot Tube .....	31
Figure 3-6: GAMBIT Model of the Three-Dimensional SPAD Body with a Blunt Nose Cone..	32
Figure 4-1: Deformation Distribution @ $p_{max}$ & F1, Section1 .....	36
Figure 4-2: Equivalent Stress Distribution @ $p_{max}$ and F1, Section one .....	36
Figure 4-3: Deformation Distribution @ $p_{max}$ and F1, Section two.....	37
Figure 4-4: Equivalent Stress Distribution @ $p_{max}$ and F1, Section two .....	37
Figure 4-5: Deformation Distribution @ $p_{max}$ and F2, Section three.....	38
Figure 4-6: Equivalent Stress Distribution @ $p_{max}$ and F1, Section three .....	38
Figure 4-7: Deformation Distribution @ $p_{max}$ and F1, Section four .....	39
Figure 4-8: Equivalent Stress Distribution @ $p_{max}$ and F1, Section four .....	39
Figure 4-9: Deformation Distribution @ F1. Base Plate .....	40
Figure 4-10: Equivalent Stress Distribution @ F1, Base Plate.....	41
Figure 4-11: Weight Saving Trade-off Study, Base Plate .....	42
Figure 4-12: Weight Saving Trade-off Study, Section two .....	43
Figure 4-13: Weight Saving Trade-off Study, Section three .....	44
Figure 4-14: Weight Saving Trade-off Study, Section four .....	45
Figure 4-15: Rubber Nose Cone Model Cross-Section .....	50
Figure 4-16: ANSYS Predicted Compression of Rubber Nose @ 40 lbs.....	50
Figure 5-1: Model of the Foam/Rubber Nose Cone Base Mold.....	52
Figure 5-2: Model of the Rubber Nose Cone Mold Insert.....	52

Figure 5-3: Cross-Section Sketches for Each Rubber Nose Fabricated. (a) The VytaFlex 50 lifted 0.5" (b) The VytaFlex60 lifted 0.2" (c) The VytaFlex60 lifted 0.6" and (d) The PMC-780 with no lift..... 55

Figure 5-4: Foam Compression Set Testing Apparatus..... 56

Figure 5-5: Foam Vertical Compression Test Apparatus ..... 57

Figure 5-6: Time to Rebound of Frozen and Room Temperature Foams..... 58

Figure 5-7: Force to Deflection Curve for Foam Noses ..... 59

Figure 5-8: Vertical Compression Test Apparatus ..... 60

Figure 5-9: Force to Deform Curves for Each Rubber Nose Cone..... 62

Figure 5-10: Failure of the PMC-780 Rubber Nose Cone..... 63

Figure 5-11:(a) The physical model is subjected to a 41.21 lbf load and deforms 0.700". (b) The ANSYS model is subjected to a 40.00 lbf load and deforms 0.730" ..... 64

Figure 5-12: Sketch of Finalized Rubber Nose Geometry..... 65

---

## List of Equations

---

Equation 2-1: Hemispherical Geometry Height .....	11
Equation 3-1: The Continuity Equation in Integral Form.....	24
Equation 3-2: The Momentum Equation in Integral Form .....	24
Equation 4-1: Thread Stress Area .....	47
Equation 4-2: Pull-Out Force per Screw.....	47
Equation 4-3: Relationship between Pressure Inside of the Inflatable to the Volume Inside the Inflatable due to a 12g CO <sub>2</sub> Cartridge.....	49



---

## List of Tables

---

Table 2-1: Spring-Loaded Nose Slide Geometry by Section.....	16
Table 2-2: Spring-Loaded Nose Cone Weights by Section .....	17
Table 3-1: Comparison of SPAD Drag Data @ $\alpha=0^\circ$ , $V_\infty=110$ mph .....	28
Table 3-2: Comparative Lift/Drag Data @ 350 mph.....	32
Table 4-1: Axial Force at $p_{\max}$ .....	35
Table 4-2: Material Properties of ABS Plastic .....	35
Table 4-3: Material Properties, Aluminum A6061 .....	40
Table 4-4: Summary of Weight Saving Optimization by Section .....	46
Table 4-5: #4-48 Screw Parameters.....	47
Table 4-6: Spring-Loaded Nose Failure Mode Analysis Results .....	48
Table 4-7: Material Properties: Natural Rubber .....	49
Table 5-1: Material Properties of Smooth-On Products .....	53
Table 5-2: Material Properties of Urethane Rubber .....	61

---

# Chapter 1: Introduction

---

## 1.1 Literature Review

Since the World War II realization that sonobuoys were the ideal detection instrument for submerged submarines, the United States Navy (USN) has used them as an integral component for their Antisubmarine Warfare (ASW) practices. Just as RAdio Detection And Ranging (RADAR) is the linchpin of military sensor equipment on and above the surface, SOUNd Navigation and Ranging (SONAR) is the eyes and ears of the military under water. While USN vessels are equipped with SONAR, the primary method for remote sensing is sonobuoy technology (OPNAV 1998). Deployable from sea-level up to 30,000 feet in altitude, sonobuoys extend sensing equipment under the sea surface and relay signal acquisition via a floating surface transmitter to the proper ASW officers without the time consuming need and risk of deploying a ship to the area.

Constructed primarily by three US companies, all sonobuoys conform to a standard set forth by current naval ASW practices. Size, shape and functionality requirements dictate sonobuoy design. As disposable assets that need to be fabricated in great quantity, manufacturing cost is a driving factor in the design. Currently, sonobuoys are stored in the Sonobuoy Launch Tube (SLT) for a foreseeable shelf life of up to five years. When duty calls, SLTs containing the sonobuoys are loaded into the launchers aboard a launch platform, currently the P-3 Orion aircraft. They are then flown to their destination where explosive charges eject the sonobuoys from the SLTs and drop them via parachute to the sea surface. Once splashed down, sonobuoys deploy underwater SONAR arrays and float transmitters on the surface. In the active phase of the

sonobuoy mission any detected target is recognized and information is relayed to the proper ASW officer. After a pre-programmed time has elapsed sonobuoys sever connections to the floating transmitters and scuttle, leaving no trace of activity (OPNAV 1998). While this Concept of Operations (CONOPS) provides a very necessary tool to the Navy, it provides three very distinct areas capable of improvement.

The increasing needs of the Navy dictate the areas of improvement in sonobuoy design. As arrays of multiple sonobuoys can provide ASW operators with significantly more useful information, there is a need for more exact equipment placement location. The conventional parachute drops are subject to missed target locations due to wind carrying descending buoys off course, miscalculations of drop locations at altitude and lack of control of the descent vehicle, the parachute. Conventional sonobuoy deployment also requires the launch aircraft to be either directly above or very near to above the target location. This means that the large, slow and rather indefensible patrol aircraft are at risk of detection and interception. As ASW is not simply a deep water initiative, capabilities to deploy sensing equipment along shorelines in littoral waters, well within RADAR and aircraft countermeasure range of potential adversaries, is a necessity (Joint Chiefs of Staff 2001). The Sonobuoy Precision Aerial Drop (SPAD) project, currently in development at KaZaK Composites, Incorporated in Woburn, Massachusetts is the solution to these increasingly compromising issues.

SPAD is a conventional sonobuoy with a modern guidance and control package. As the next step in ASW technology, SPAD can place a sensor package on the ocean surface with high-tech precision and stealth. The addition of the guidance and controls package means that no longer do sonobuoys need a nearly vertical deployment trajectory but launch aircraft can remain at a

standoff range and place sensors up to 39 nautical miles away. Programmable waypoints in the guidance system can assure that SPAD evades any enemy detection equipment providing little to no knowledge of USN sensor equipment in the water.

The SPAD Aerial Deliver Vehicle (ADV) is mated with a conventional g-sized sonobuoy and stowed in a SLT concurrent with all ASW practices. Where previous conventional drops would require the P3 launch vehicle to fly directly to the destination, the SPAD program CONOPS requires the P3 to fly up to altitude within range of the target and fire the same explosive charge jettisoning SPAD from the SLT. The next stage of the mission replaces the conventional parachute drop. SPAD gains velocity and deploys its control surfaces. As an unpowered glider SPAD follows its GPS guided flight plan and reaches its target. Above the target location the SPAD initiates a sonobuoy jettison maneuver clearing the ADV from the trajectory of the, now uncontrolled, sonobuoy. At the point of separation the sonobuoy drop follows the conventional para-drop procedure. Figure 1-1 and Figure 1-2 show the SPAD assembly on the following page.

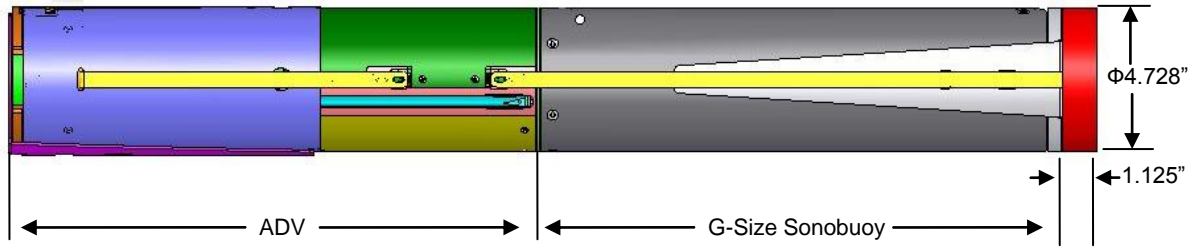


*Figure 1-1: SPAD in compressed storage stage*

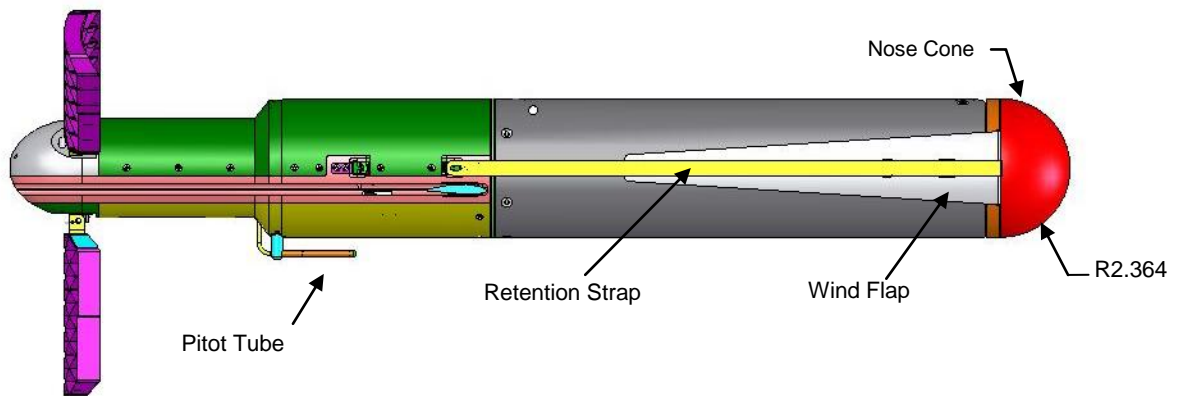


*Figure 1-2: SPAD in extended flight configuration*

## **1.2 Project Objectives, Requirements and Approach**

### ***Objectives***

As an unpowered glider the SPAD design has an emphasis on the minimization of drag. This requires certain streamlined shapes for the vehicle surface. This geometrical requirement dictates shapes and sizes; however SPAD still has to fit within the restricted geometry of the SLT.

Breaking the vehicle up into two components; the sonobuoy, which is an off the shelf system that cannot be altered in length, shape or size and the ADV which is geometrically comprised of the wings and control surfaces, the ADV is the only component whose geometry can be altered. To maximize the wing area, the wingspan must be maximized and thus the ADV must be at its maximum allowable length. With a predetermined overall length this leads to a lack of room for a streamlined nose cone. A design solution for a nose cone, that can pack within the available geometry of the SLT yet retain the larger, drag minimized shape for flight is needed.

### ***Requirements***

As much of SPAD has already been designed and tested, wind tunnel analysis values that provide lift, drag and moment coefficient for stability derivatives, which effect autopilot response, have already been resolved. These stability controls would be costly to change. This means that the SPAD wind tunnel model cannot be significantly changed without great cost to the project. In order to maintain these wind tunnel values, unless analysis provides a better solution, the nose cone must weigh, more or less, 0.36 pounds and must be hemispherical in shape with a radius of 2.364 inches. The SPAD maximum design velocity is 350 miles per hour (mph). As low speed wind tunnel testing topped out at 110 mph, test data must be resolved at the maximum flight speed. This will provide values for pressure distributions over the nose cone in flight giving a design requirement for structural stability. Preliminary data shows maximum

pressure as 2.5 psi. The nose cone structure must not significantly deform under these flight pressures. Significant deformation would be defined as anything that would affect the laminar flow over the airframe and its control surfaces or increase the drag forces. Analysis must also confirm that the nose cone design will not seriously effect Pitot tube location. The Pitot tube is located 0.55” away from the SPAD surface; its location in the free stream must be confirmed as the guidance system relies heavily on this device. The nose cone must have an attachment interface to the sonobuoy wind flap, be able to survive a concussive launch shock of up to 20 Gs and operate in a temperature range of -40° F to +135° F. As the inactive shelf life of sonobuoys is 5 years, the design must remain viable for that period of compressed storage. Finally, as cost is the driving factor in all projects but most specifically those that are high in quantity and disposable, the nose cone must be capable of acquisition for a cost of fewer than 25 US dollars.

### ***Approach***

In order to design, analyze, fabricate and test possible nose cones for SPAD, the following approach was taken:

1. Produce four design concepts, fundamentally different in nature, which meet the project requirements.
2. Produce an aerodynamic analysis of the flow around the SPAD body.
3. Produce a structural analysis for each of the nose cone concepts resulting in rejection and discontinuation of failing concepts.
4. Fabricate and physically test the remaining nose cone concepts resulting in a final rejection and discontinuation of failing concepts.
5. Summarize the data gathered and conclude the best candidate for the SPAD nose cone.

In order to produce the aerodynamic analysis about the SPAD body, the following approach was taken:

1. Import the SPAD body geometry into the meshing software GAMBIT. By removing small discontinuities in the SPAD surface, create a simplified, but similar, SPAD body increasing solution speed.
2. Mesh the flow volume and create the boundary conditions in GAMBIT.
3. Import SPAD GAMBIT file into the numerical solver FLUENT and create a dynamically similar environment to that of the 110 mph wind tunnel tests.
4. Verify the model accuracy by comparing numerically solved data with wind tunnel recorded data.
5. Increase flow to SPAD maximum design speed and resolve the drag force, lift force, total pressure distribution about the nose surface and the thickness of the viscous boundary layer in the vicinity of the Pitot tube.
6. Evaluate the total pressure distribution about the nose for use in the structural analysis.
7. Evaluate the measured thickness of the viscous boundary layer to verify Pitot tube location in the free stream flow.
8. Return to GAMBIT and create SPAD body with a blunt nose and mesh the flow volume in the same manner as the original SPAD body to remove any meshing derived inconsistencies.
9. Import the blunt nose SPAD into FLUENT and run analysis with identical conditions to that of the hemispherical SPAD maximum speed analysis and resolve the blunt nose SPAD drag forces and lift forces.
10. Evaluate and compare the lift/drag data for the blunt nose SPAD and the hemispherical nose SPAD. Verify the need for a hemispherical nose cone.



In order to produce the structural analysis of each nose cone concept, the following approach was taken:

1. Determine the manner in which flight loads and storage loads will be applied to each design concept and determine the manner in which the concepts can be analyzed numerically.
2. Evaluate the structural integrity in the FEA solver ANSYS, for concepts capable of numerical analysis, loaded with flight and storage forces.
3. Evaluate the remaining concepts capable of numerical analysis using a computational method for structural integrity.
4. Reject and discontinue any concept which fails to meet the design requirements based on the gathered data.

In order to fabricate and physically test the remaining nose cone concepts, the following approach was taken:

1. Determine which nose cone concepts need to be fabricated based on data already collected and determine manner in which each nose cone concept can be fabricated.
2. Produce prototype models.
3. Produce tests results for time to rebound and completeness of rebound by compression set testing at variable temperatures.
4. Produce tests results for compression testing, comparable to the numerical test methods in the structural analysis section.
5. Verify numerically solved compression test data with physical compression test data.
6. Reject and discontinue any concept which fails to meet the design requirements based on the gathered test data.

---

## Chapter 2: Nose Cone Design

---

In attempt to design, fabricate and test a reliable nose cone within the limited time provided, four different nose cones were conceptualized. This allowed time to be spent on improving good design concepts rather than attempting to fix fundamentally faulty concepts. Four concepts were made utilizing different structural designs, mechanics and material properties. The first of these was a rigid, collapsible, mechanical structure which utilized the strength properties of rigid materials. The second concept attempted to create a no-stress storage environment by the use of an inflatable device. The final two designs attempted to employ the unique elastomeric characteristics of urethanes. One of these designs relied on the strength, as well as the elasticity of solid urethane rubber. The last of the design concepts was focused on the compressibility, and resiliency, of urethane foam rubber. They are described in detail as follows.

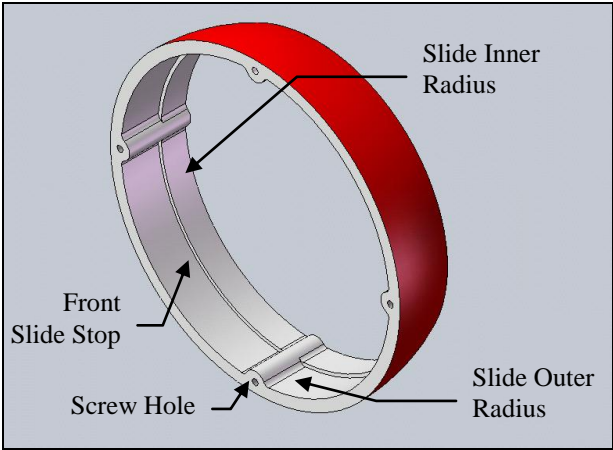
### 2.1 Spring-Loaded Nose

The Spring-Loaded Nose employs the use of a spring-loaded four tier collapsible system that extends to a designed height and compresses within the area of the first tier. As ABS plastic and Aluminum alloy are the materials selected for the structural segments, this design offers a high strength to weight ratio. With specifically engineered low solid thickness, high spring constant wave springs; the structure can retain its shape against flight pressures of almost any airspeed.

#### 2.1.1 Section One

Figure 2-1, shown on the following page, shows the first section of the nose cone geometry.

Allowing room for base plate thickness the section height is very important as all subsequent sections need to fit within this geometry. A 1” height was chosen, allowing adequate room for the base plate while maximizing the area for the other nose cone sections.



**Nose Section One**

<b>Material</b>	ABS Plastic
<b>Weight</b>	0.066 lbs
<b>Effective Surface Area</b>	14.853 in <sup>2</sup>
<b>Height</b>	1.0 in
<b>Design Spring Load (F1)</b>	50 lbs
<b>P<sub>max</sub></b>	2.5 psi

***Figure 2-1: Spring Loaded Nose, Section One***

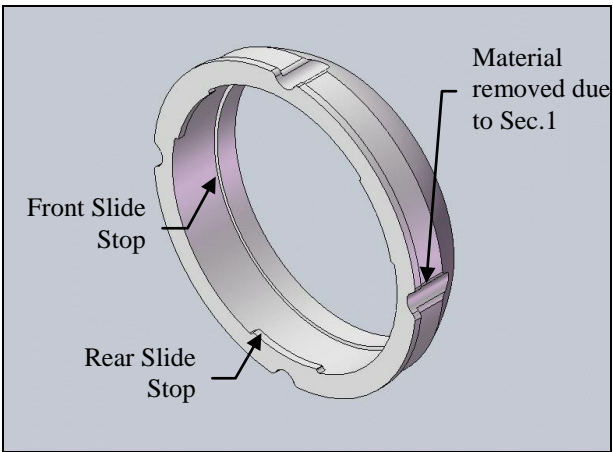
Four screws are sunk into the back side of section one providing a fixture to the base section. Because of the necessary forces in the system larger screw diameters are needed to provide the proper support. This leads to a build up of material around the screw hole locations. While the screws are not 1” long this material was continued to the front end of the section to provide sliding support for the system as well as to maintain a smooth, continuous surface on the outside face to promote laminar flow effects.

A lip extends into the inner radius at the front end to provide a slide stop to contact section two. There is no rear slide stop as section one lies flush against the base plate. The radius of curvature of the hemisphere is centered along the center axis coincident with the rear plane of section one. All subsequent radii reference this point in the assembly.

***2.1.2 Section Two***

Section two of the assembly is designed to sit flush with the base section while in full compression and therefore can be 1” in height, just as high as section one. The equal heights of sections one and two fill the maximum height set forth in the design requirements while still

allowing room for subsequent section geometry. When fully extended the rear slide stop of the section is designed to rest in contact with the front slide stop of the previous section.



**Nose Section Two**

<b>Material</b>	ABS Plastic
<b>Weight</b>	0.096 lbs
<b>Effective Surface Area</b>	7.103 in <sup>2</sup>
<b>Height</b>	1.0 in
<b>Design Spring Load (F1)</b>	50 lbs
<b>P<sub>max</sub></b>	2.5 psi

**Figure 2-2: Spring Loaded Nose, Section Two**

Shown in Figure 2-2, the outer radius of section two is defined by the slide available outer radius of section one; as is the inner radius by the slide available inner radius. From there the cone geometry can be constructed.

Keeping in mind the available slide distance provided by section one, the hemisphere height of section two can only equal the available slide distance minus the rear stop length.

$$h_{h_n} = d_{s_{n-1}} - l_{r_{s_n}}$$

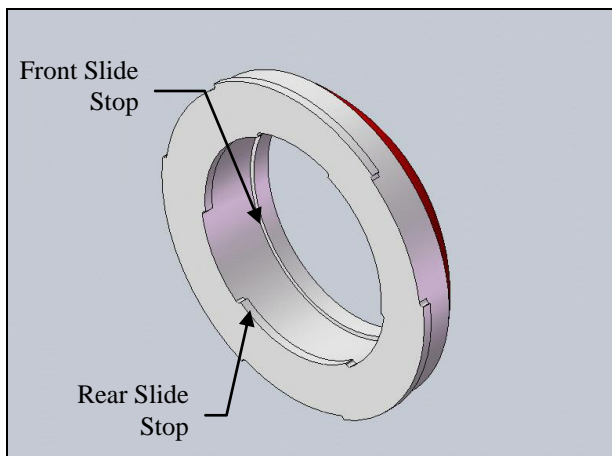
**Equation 2-1: Hemispherical Geometry Height**

To fit within the geometry of section one, material from section two is to be removed from the areas where the screw supports are located in section one. These extrusions in section one provide a beneficial side effect in that they create a rail for section two to ride on which counteracts twisting inside of the assembly.

Section two is also equipped with a slide stop at the front end of the slide. However, this section introduces the use of a rear slide stop. While this slide stop is necessary to prevent an unintentional removal from the slide system of section three from section two, it takes much needed space away from the slide distance; reducing the overall hemisphere height of the subsequent section. Notches have also been removed from this slide stop to provide an installation technique for the subsequent section.

### 2.1.3 Section Three

Section three, shown in Figure 2-3, is designed to rest flush with the front of the rear stop of section two when in full compression. Because of this reduced slide distance caused by an elevated rest height, there is less available clearance for the hemisphere.



#### Nose Section Three

<b>Material</b>	ABS Plastic
<b>Weight</b>	0.125 lbs
<b>Effective Surface Area</b>	7.352 in <sup>2</sup>
<b>Height</b>	0.9 in
<b>Design Spring Load (F1)</b>	50 lbs
<b>P<sub>max</sub></b>	2.5 psi

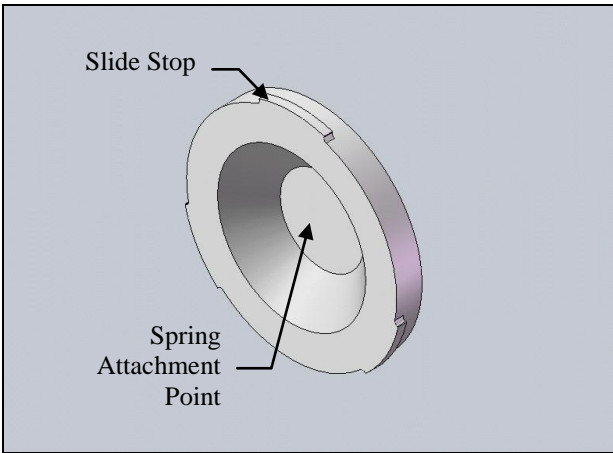
**Figure 2-3: Spring-Loaded Nose, Section Three**

When fully extended the rear slide stop of this section is also designed to rest in contact with the front slide stop of the previous section. Notches have been removed from the slide stops to provide installation to the previous section. A simple insertion and twist locks section three within the slide stops of section two. There is no rail system as in section two to provide

rotational support, as forces will be loaded axially significant rotation forces should not be incurred.

**2.1.4 Section Four**

Section four is the final stage of the nose cone assembly. Because of the maximization of the previous three sections geometry, section four can remain relatively small. This small size is beneficial as the compression spring is required to fit within the area provided by the distance between the base plate and section four when fully compressed.



<u>Nose Section Four</u>	
<b>Material</b>	ABS Plastic
<b>Weight</b>	0.069 lbs
<b>Effective Surface Area</b>	5.366 in <sup>2</sup>
<b>Height</b>	0.303 in
<b>Design Spring Load (F1)</b>	50 lbs
<b>P<sub>max</sub></b>	2.5 psi

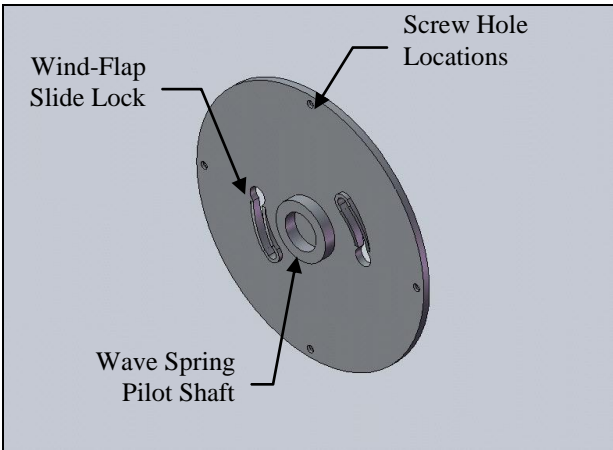
**Figure 2-4: Spring-Loaded Nose, Section Four**

Shown in Figure 2-4, section four is equipped with a slide stop about the slide radius. This prevents an accidental removal from the slide system rear as well as a stop height for full extension. The backside of section four also provides a flat surface forming an area for the compression spring to rest in. The height of this point at full compression is very important as it cannot be smaller than the solid height of the spring.

**2.1.5 Base Plate**

Shown in Figure 2-5, the base plate is a very important component of the overall assembly. All of the loading from the hemispherical sections will be applied on this section. This means the

base plate must be able to resist the maximum force applied by the compression spring at any possible compression state as well as the forces exerted on the outside geometry cause by the dynamic pressures of flight.



**Base Section**

<b>Material</b>	Aluminum A6061
<b>Weight</b>	0.223 lbs
<b>Effective Surface Area</b>	1.62 in <sup>2</sup>
<b>Height</b>	0.135 in
<b>Design Spring Load (F1)</b>	50 lbs
<b>p<sub>max</sub></b>	2.5 psi

***Figure 2-5: Spring-Loaded Nose, Base Plate Section***

Because of the high loads concentrated on the base plate, ABS plastic is unsuitable as the strength and deformation properties simply do not meet the requirements. Aluminum alloy A6061 was chosen as the lightweight, high strength material to use in the place of ABS plastic. 6061 aluminum was chosen as it is a common aerospace material that is lightweight, strong and stiff. The material properties of A6061 allow the base plate to be very thin. This quality is important as the available height for the base plate is only 0.125”.

The base plate has a constant diameter, sized to fit the maximum diameter of the section one. Counter bored screw holes are located along an outer radius of the plate to form the attachment with section one. A circular extrusion in the center of the base plate supports the compression spring. Along a radius outside that of the outside radius of the compression spring there are two slots. These slots provide an attachment point to the wind flap of the sonobuoy. Currently the sonobuoy has retention straps that are locked into place by machine screws. These machine

screws are to be replaced by machine shoulder screws. These shoulder screws will provide an area for the base plate to attach. The base plate is designed to accept the shoulder screws inside the base and upon rotation about the shared axis lock into place. The shoulder screw locks are simple ramps with a physical barrier to allow one directional rotation. After the base plate is fully rotated 45 degrees, a force greater than any exerted during a storage or active phase is required to rotate the opposing direction. This attachment is shown in Figure 2-6.

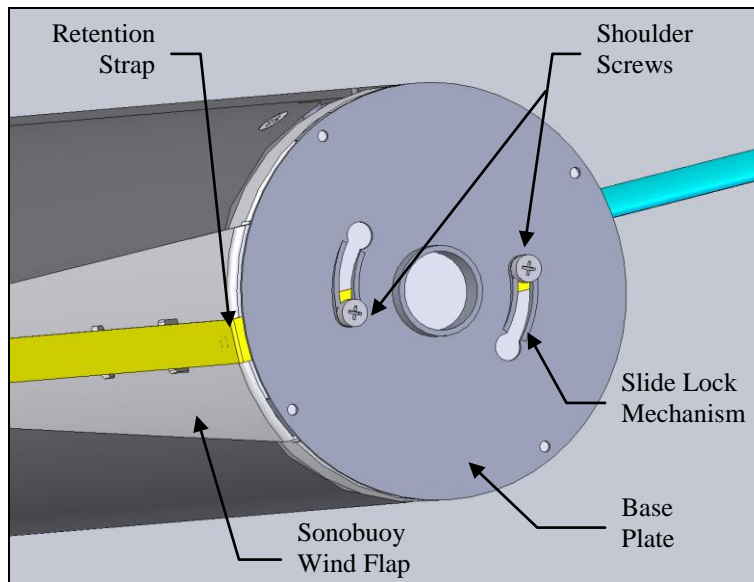


**Figure 2-6: Base-Plate to Sonobuoy Wind Flap Connection**

### **2.1.6 Spring-Loaded Nose Assembly**

While Figure 2-1 to Figure 2-5 show the collapsible sections and base plate of the spring-loaded nose cone, Figure 2-7 on the following page shows the full assembly. As said previously, section four fits inside of section three, section three fits inside of section two and so on. Each of the connections between sections are sliding connections with end stops at the forward and aft ends of the groove. Section one can be seen connected to the base via the 4 machine screws. Between the base plate section and section four there is a wave compression spring. Wave compression springs are important to the design as they offer a very high force exertion from a very small



physical area compared to a normal compression spring. Wave springs can compress to the 0.7” length provided by the assembly and extend to a 2.07” length while still exerting the required 50 lbf.

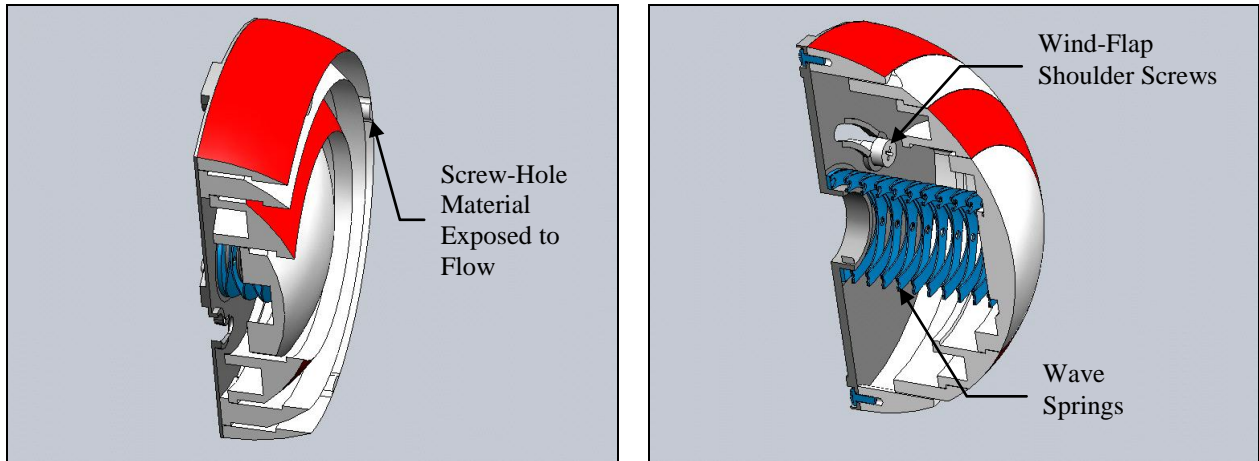


**Figure 2-7: Spring-Loaded Nose, Assembly at Full Compression and Total Extension**

Table 2-1 shows the relationship between inner and outer radii as well as slide distances for the assembly. These relationships are crucial to maintain spherical geometry.

<b>Section</b>	<b>Height</b>	<b>Available Slide Distance</b>	<b>Front Stop Length</b>	<b>Rear Stop Length</b>	<b>Outer Radius</b>	<b>Inner Radius</b>	<b>Slide Available Outer Radius</b>	<b>Slide Available Inner Radius</b>
<b>1</b>	1.000	0.6	0.4	-	-	-	2.192	2.142
<b>2</b>	1.000	0.6	0.3	0.1	2.188	2.138	1.877	1.827
<b>3</b>	0.900	0.6	0.2	0.1	1.873	1.823	1.311	1.261
<b>4</b>	0.303	-	-	1.306	1.256	-	-	-
* all dimensions are in inches								
** inner and outer radii reflect a 0.002 tolerance								

**Table 2-1: Spring-Loaded Nose Slide Geometry by Section**

Table 2-2 shows the weight of each section in tabular form. The current total weight is exceeding the design requirements by 61%. A weight optimization must be completed in the design analysis phase or else SPAD could become unstable in flight.

<b>Description</b>	<b>Weight (lbs)</b>
Section 1	0.066
Section 2	0.096
Section 3	0.125
Section 4	0.069
Base Plate	0.223
<b>Total</b>	<b>0.579</b>
<b>Design Requirement</b>	<b>0.360</b>
<b>Weight Excess</b>	<b>0.219</b>

*Table 2-2: Spring-Loaded Nose Cone Weights by Section*

## 2.2 Inflatable Nose

### 2.2.1 Inflatable Nose Assembly

The Inflatable Nose design is one of extremely minimized storage volume. However, adding to the complexity it is made up of many individual components. In keeping with a cost minimized design, the inflatable nose is centered around an off the shelf component, the compressed CO<sub>2</sub> cartridge. The inflatable nose design is shown in Figure 2-8. While in the storage phase of the mission the inflatable nose is to rest on the base plate structure. When entering the active flight phase the inflatable nose is to be turned on via a pressure switch. The activation of this pressure switch opens a connection between a battery and a resistor. The resistor then burns a cut-line holding back a trigger spring. When released the trigger spring pierces a pressurized gas bottle inflating the nose. Figure 2-8 shows the inflatable nose assembly on the following page.

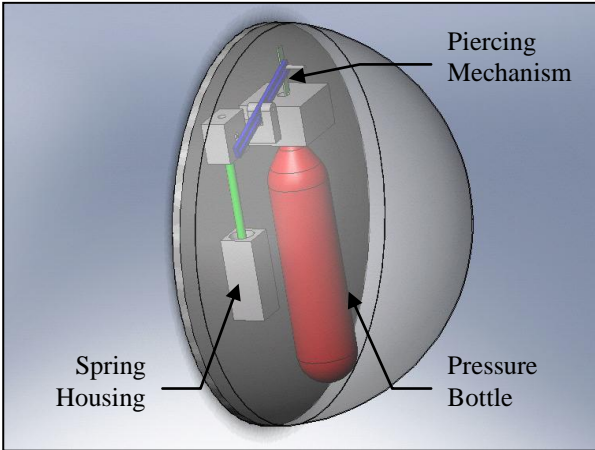


**Figure 2-8: Inflatable Nose Assembly (Pressure Switch Not Shown)**

### **2.2.2 Base Plate**

The inflatable nose base plate is the largest component of the system. The design of the base plate is to hold all the subsequent components in place as well as provide rigid support for the assembly. Shown in Figure 2-9, the base plate is comprised of the gas bottle connection, the firing pin swing arm hinge and the spring housing. The attachment point must differ from the previous nose cone design as the inside volume of the inflatable must be pressure sealed from the outside.

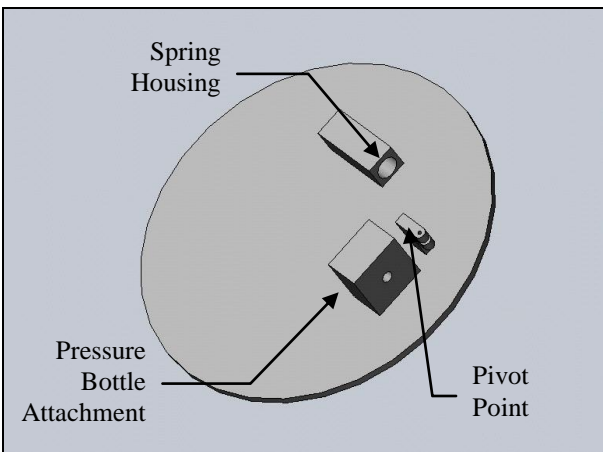


**Figure 2-9: Inflatable Nose Base Plate**

To reduce cost, the base plate is to be one of the only parts to be manufactured for this assembly. ABS plastic was chosen as the material for this section for its strength and weight properties. As the base plate is not directly loaded by any forces of great magnitude the weight, strength and stiffness of ABS is ideal.

### ***2.2.3 Inflatable Balloon***

The inflatable balloon, as seen as the transparent component in Figure 2-8 on the previous page, is to be the second of the two components manufactured specifically for this application.

Constructed from a polymer material this very thin, very lightweight balloon will support all the loads of the nose while in flight. As the balloon is to be attached to the base plate to form a pressure seal, special focus must be given to this region as integrity must be maintained for the duration of the flight phase. Any loss of pressure would be catastrophic for the SPAD flight performance. Analysis will provide ideal attachment location and method.

### ***2.2.4 Pressurized Gas Bottle***

The pressurized gas bottle, shown in Figure 2-10, is the centerpiece of this design. To limit cost, the component is designed to be an off the shelf integration. Standard 12g CO<sub>2</sub> bottles can be purchased from a variety of distributors.

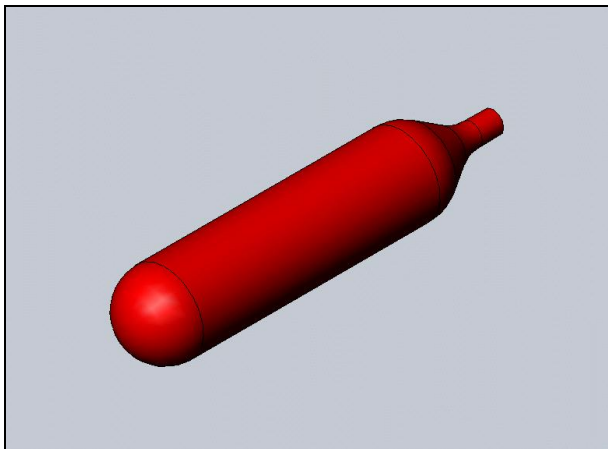


***Figure 2-10: Pressurized CO<sub>2</sub> Gas Bottle***

At a standard size of 3.5" x 1", these bottles can be integrated into the assembly very easily. The gas bottle is designed to fit within an attachment on the base plate. No gasket is necessary as the compressed volume is to expel into the sealed nose chamber.

### 2.2.5 Trigger Assembly

The trigger assembly is one of the most complex components of this design. Shown in Figure 2-11, the trigger employs the use of a pressure switch to keep the system disarmed while in storage. Upon exiting the launch tube the pressure switch is disengaged and current is able to flow from a 9 volt battery to a 2 ohm resistor. The resistor is placed in close proximity to a twine retention string. This retention string holds back the force of a compression spring. When the resistor is supplied with current it heats up, cutting the retention string and sending the compression spring outward. Prior proven use of a resistor heating element for this application has been found in sonobuoy design. When the compression spring is extended it forces a pin to pierce the pressure bottle exhausting pressurized gas into the balloon chamber. Analysis will provide values for pressure within the inflatable chamber as well as values for compression spring constant.

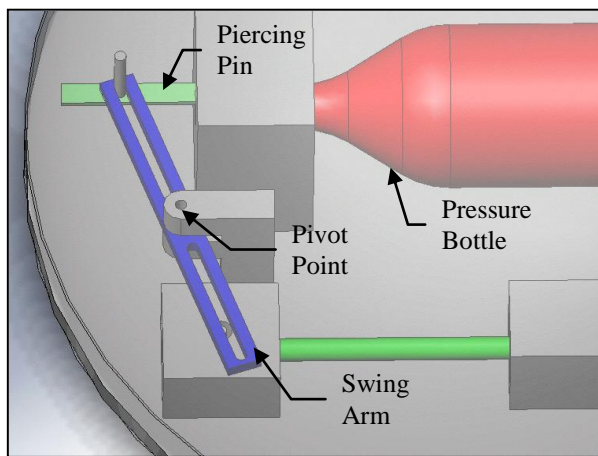


**Figure 2-11: Inflatable Nose, Trigger Assembly**

### 2.3 Rubber Nose

The Rubber Nose is completely dependant on the elastomeric structural and material properties of solid urethane rubber. As natural and synthetic rubbers have long been used as materials for controlled deformation in all sorts of temperatures and pressures, they are a proven material for this application. For this design the rubber nose structure must be able to compress to approximately 50% of its original height. For this much deformation a solid piece of rubber is unsuitable as the forces would be too great for compression and the deformation undesirable. In order to demonstrate the required deformation effects at the specific forces the rubber needs to be hollowed out as shown in Figure 2-12.

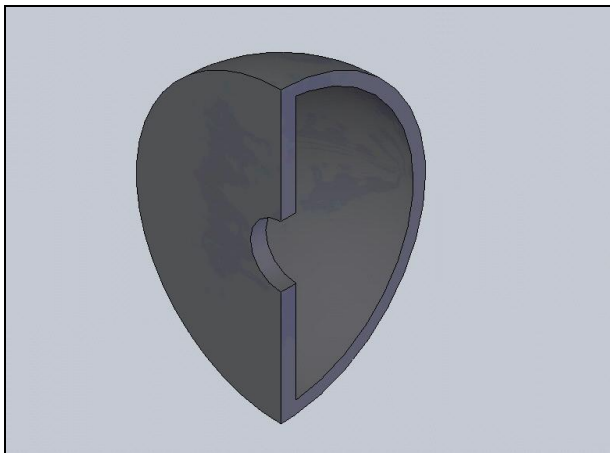


***Figure 2-12: Rubber Nose (Wind-Flap Attachment Not Shown)***

In order to provide the proper deformation characteristics the rubber nose is designed to be structurally sound at the maximum pressures about the outside surface in flight. Any excess of the maximum flight pressure will cause a controlled structural failure in the form of buckling. This is the basis of the design for the rubber nose to pack within itself.

In order to design this controlled buckling, analysis will provide optimal sidewall thickness and geometry. Once compressed the elastomeric properties of the urethane rubber will allow the

structure to rebound without any lasting geometrical changes or permanent material failures.

Attachment to the wind flap will be made via the same shoulder screws as in the spring design.

## 2.4 Foam Nose

The Foam Nose design is based on the elastomeric properties of urethane foams. As foam density and elastic properties can almost be made-to-order, a foam nose could be a viable option for its simplicity of manufacturing and basic operation. As foam is much less dense when compared to rubber, the foam nose will be constructed out of a solid piece of foam and deformation will be resisted by foam material properties alone. Foam is not marketed based on numerical properties such as elastic modulus or Poisson's ratio so different foams must be experimentally tested for their compressive capabilities for analysis.

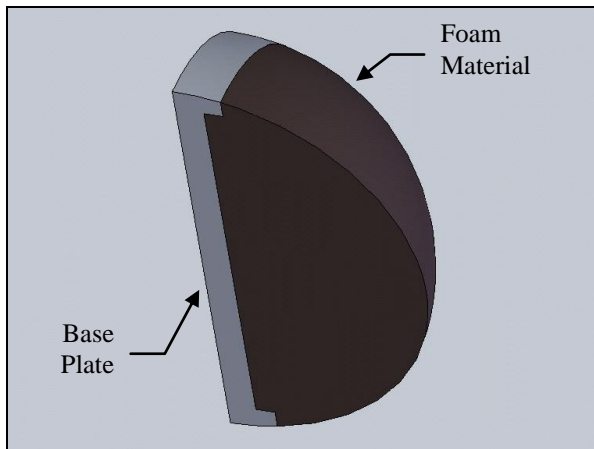


**Figure 2-13: Foam Nose Assembly**

Shown in Figure 2-13, the foam nose assembly is to be a solid piece of molded foam adhered to a base plate. This plate is to fit the geometry of the surface of the hemisphere for continuity. Once adhered to each other the assembly is to be locked in place on the top of the wind flap via the same shoulder screws as the rubber and spring designs.

---

## Chapter 3: Aerodynamic Analysis

---

The primary mission of SPAD is that of a flight vehicle. It is in this environment that the structure encounters its primary loading. Due to the viscous stresses and pressures of fluid flow, these load cause the collapse, and ultimate failure, of any nose cone design (Anderson 2007).

The viscous effects of air create a boundary layer separating regions of zero flow velocity to full flow field velocity causing pressure drag, and in this application potentially inaccurate Pitot tube measurement (Pope 1966). It is because of these very dynamic effects that the aerodynamics of the SPAD must be analyzed. In order to create a structure that can withstand the pressures of an incoming air flow the total pressure distribution about the SPAD body must be calculated. As a final proof of concept the SPAD hemispherical nose will be compared to a blunt nose at maximum speed demonstrating the essential need for a streamlined nose cone.

### 3.1 Methods

The method used in the analyses will be a Computational Fluid Dynamics (CFD) modeling software, FLUENT. CFD numerical solvers have taken over as the primary first stage in aerodynamic analysis (Anderson 2007). While bench top, wind tunnels and prototype testing are still necessary in aerospace R&D much of the initial analysis can be modeled using numerical solvers. CFD programming is rooted in the flow equations of fluid dynamics. Since SPAD is a subsonic aerial vehicle, the flow is to be treated as an un-steady, three-dimensional, incompressible, viscous flow. As the temperature is expected to change only by small increments the flow can be defined by the Navier-Stokes equations of momentum and the continuity equation alone. The energy equation would be introduced if compressibility effects were to be taken into account. However, at low mach numbers air can be treated as incompressible



(Anderson 2007). As the SPAD maximum design speed is mach 0.45 it is entering the arbitrarily assigned compressible regime. Since this is the maximum speed of SPAD and it is only entering the compressible regime, analysis treated air as incompressible for simplicity.

Continuity equations are employed as numerical representations of what has been found to be fundamental laws of modern physics.

$$\frac{\partial}{\partial t} \iiint_V \rho dV + \iint_S \rho \mathbf{V} \cdot d\mathbf{S} = 0$$

**Equation 3-1: The Continuity Equation in Integral Form (Anderson 2007)**

These equations state that within a closed system there is mass and energy and they are constant. In the application of fluid dynamics, the continuity equation states that the rate of mass entering the system is the rate at which mass leaves the system. Shown in Equation 3-1, the continuity equation states that the net mass flow out of the system is equal to the time rate of decrease of mass inside the system. The above form represents the continuity equation for flows in general. Terms can be removed and the equation simplified depending on the parameters of the flow.

$$\frac{\partial}{\partial t} \iiint_V \rho \mathbf{V} dV + \iint_S \rho \mathbf{V} \cdot d\mathbf{S} \bar{\mathbf{y}} = - \iint_S p d\mathbf{S} + \iiint_V \rho \mathbf{f} dV + \mathbf{F}_{viscous}$$

**Equation 3-2: The Momentum Equation in Integral Form (Anderson 2007)**

The momentum equation, shown in Equation 3-2 on the previous page, is derived from Newton's Second Law of Motion, **Force** = mass x **acceleration** ( $\mathbf{F} = m\mathbf{a}$ ). Applied to fluid dynamics the equation states that total forces,  $\mathbf{F}$ , equal the total time rate change of momentum,  $\frac{d}{dt}(\rho \mathbf{V})$ . From the momentum equation follows the Navier-Stokes Equations. Solving these equations with the continuity equation provides the solution to the fluid flow field (Anderson 2007). The solution to the momentum and continuity equations, when solved simultaneously, will provide information for the flow around the SPAD to be analyzed.

### 3.2 Procedure

These aerodynamic analyses will be performed in three stages. The first stage will confirm wind tunnel testing values. This will provide proof that the analysis is concurrent with real physical data. Since the wind tunnel data was taken at a flow velocity of 110 mph, this is the flow speed selected for the first analysis. Drag values from the wind tunnel are to be compared with drag values provided by CFD analysis at 110 mph. The second stage will analyze SPAD in a flow of the maximum designed velocity of 350 mph. Lift and drag data will be recorded. Pitot tube location will also be confirmed within the free stream. Most importantly for this section however; the pressure distribution about the nose cone will be recorded. This will provide the maximum pressure value that the nose cone will encounter in flight. From there a maximum structural strength can be designed into the nose cone to minimize the compressed storage forces. Lastly, SPAD with a hemispherical nose will be compared to a blunt nose SPAD at maximum velocity. This will confirm the need for a specifically designed streamlined nose. Lift and drag

data will be recorded from this analysis showing that range and maximum velocity would be adversely affected in the case of a blunt nose SPAD.

In order to accomplish the above procedure the SPAD model must first be constructed in the computer environment. To do this the software GAMBIT, which is packaged with FLUENT, was used. GAMBIT allows physical models to be created in the virtual environment. Another specific function of GAMBIT is to mesh the computer model. Meshing is very important to computer analysis. As analysis requires fluid flows to be broken up into small elements, mesh is the term describing and controlling the size and shape of these finite elements. For this particular analysis SPAD was constructed in three-dimensional space. To do this the SPAD body model was first imported into GAMBIT. Once in GAMBIT, SPAD was meshed. In order to aid in the solution time the surface mesh on the SPAD was elected to be rather coarse. From there a flow volume was created, shown in Figure 3-1.

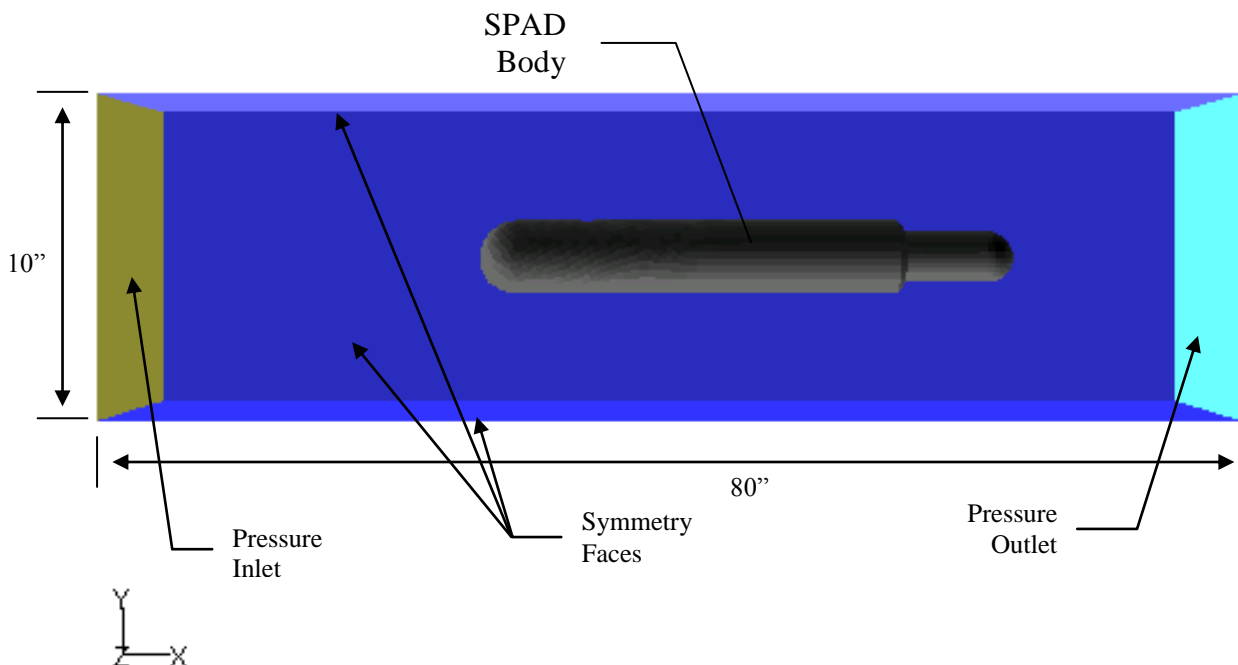


**Figure 3-1: GAMBIT Model of the Three-Dimensional SPAD Body with a Hemispherical Nose Cone**

The flow elements were finest right up to the SPAD body, 0.005 inches long. A size function was created increasing the size of the mesh as the distance from the SPAD increased. In order for the CFD solver to calculate boundary conditions, pressure inlets and outlets were defined as well as the surrounding faces to be defined as symmetry faces and the SPAD was defined as a wall. Defining faces as pressure inlets and outlets do exactly what they describe; they provide the solver with a boundary condition for pressures which create a flow direction. Symmetry faces create a slip condition. As the flow must be contained in a control volume for the equations of fluid dynamics such as continuity and Navier-Stokes to yield solutions, symmetry faces contain the flow volume within a bounding box while not allowing the effects of viscosity to be represented on their faces. With the flow defined the mesh was created and exported into the solver.

Once in the numerical solver the SPAD model had to be placed in the proper flow environment. As SPAD is essentially a low velocity glider the flow was defined as a three-dimensional, unsteady, viscous flow. In order for ease of solution the altitude was fixed at sea level providing a  $P_{\text{Atmospheric}}$  of 14.7 psi (Anderson 2007).

### **3.3 Results**

This section explores the solution to each of the three CFD analysis runs. Raw data was compiled and illustrated in figures or tabular form for simplicity.

#### **3.3.1 Conformity Analysis**

The first CFD solution of the SPAD was run at a flow velocity of 110 mph. This provided a dynamically similar environment to the data collected by KCI at the MIT Wright Brothers Wind

Tunnel in Cambridge, Massachusetts which is shown in Figure 3-2 on the following page. In this analysis drag data is compared from both the numerical solution and the raw test data.

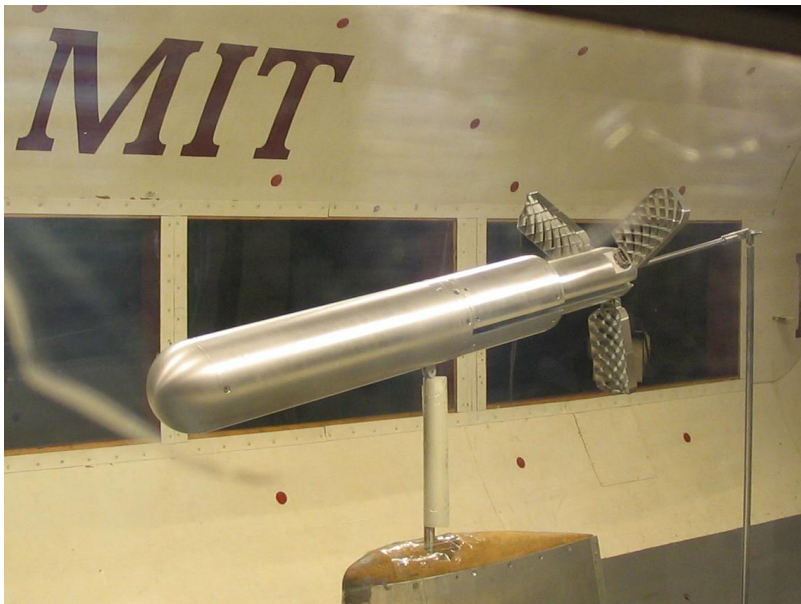


**Figure 3-2: SPAD Wind Tunnel Model with Control Surfaces Attached and Deployed in MIT's Wright Brothers Wind Tunnel (Courtesy of KaZaK Composites, Inc.)**

	<b>Drag (lbs)</b>
<b>Wind Tunnel Value</b>	0.35
<b>FLUENT Value</b>	0.34

**Table 3-1: Comparison of SPAD Drag Data @  $\alpha=0^\circ$ ,  $V_\infty=110$  mph**

The above Table 3-1 shows the comparison of the drag data collected from the two different processes, a physical flow environment and a virtual flow environment. Not that CFD requires validation, however for this application it confirms that the computer model represents physical model accurately.

### **3.3.2 Maximum Velocity Analysis**

After the accuracy of the CFD model was confirmed, the second run provided an analysis for the SPAD at its maximum design velocity. This produced the required lift and drag data, but more importantly a view of the pressure distribution about the surface of the nose cone. Figure 3-3 on

the following page shows this distribution. The nose cone was 2.364 inches in radius, so the figure shows values from the tip of the nose cone, 2.364 inches, to the base of the nose cone, 0 inches. As preliminary data approximately predicted, the maximum total pressure that the nose cone encounters is 2.4 psi. This pressure distribution provides loading criteria for structural analyses of the nose cone.

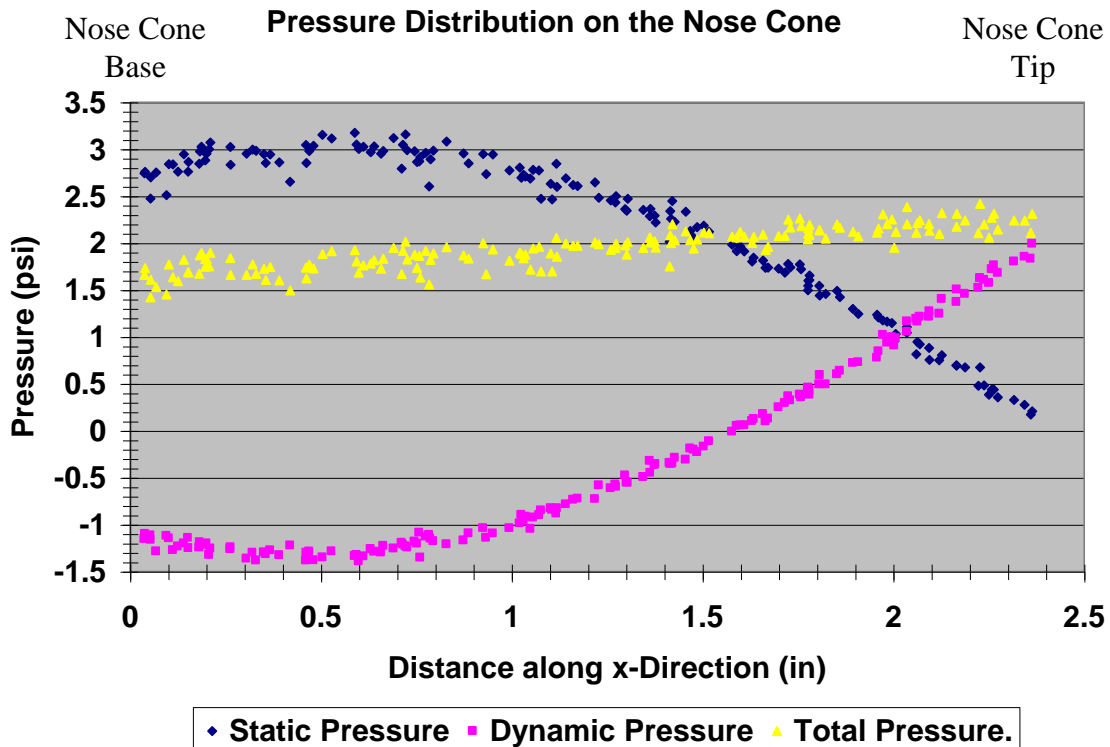


**Figure 3-3: CFD Derived Values for SPAD Nose Cone Pressure Distribution @  $\alpha=0^\circ$ ,  $V_\infty=110$  mph**

The pressure distribution can also be displayed on the SPAD body itself. Together with the x-y plot, the pressures experienced by SPAD at maximum design velocity can be interpreted. Figure 3-4 on the following page shows SPAD with static pressure contours about the body.

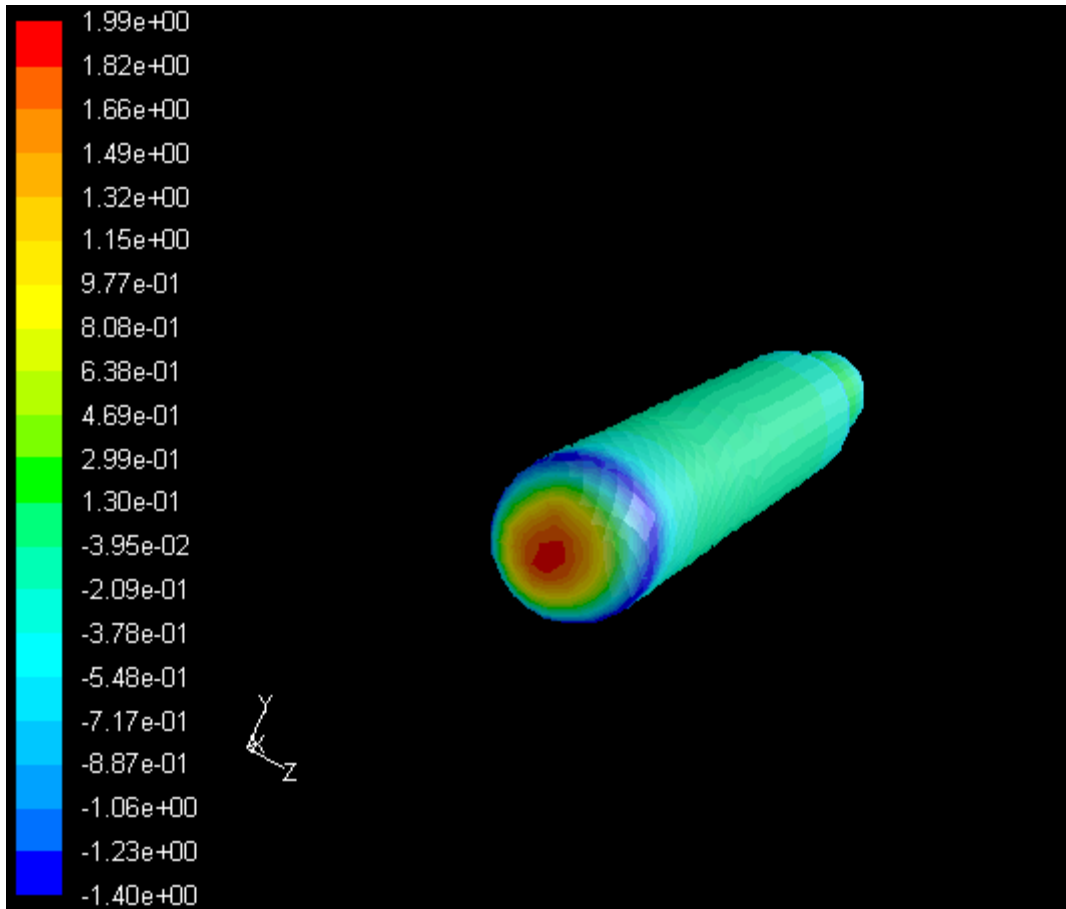


**Figure 3-4: Pressure Distribution about the SPAD Body @  $\alpha=0^\circ$ ,  $V_\infty=110$  mph**

The above figure clearly shows that the highest pressure experienced by the SPAD nose cone is focused at the center of the nose. From there the pressure quickly diminishes. When combined with the dynamic pressure the total pressure is resolved.

The Pitot-tube location was also confirmed in this analysis. By mapping the velocity magnitude from the surface of the SPAD body outward an approximate thickness of the viscous boundary layer can be measured and the free stream can be located. This method can prove that the Pitot tube is in the free stream (Schlichting 1968). The plot shows the velocity magnitude referenced by the origin at the center of curvature of the SPAD body. Since the radius of the SPAD body

was 2.364”, the Pitot tube is located at 2.914”, 0.55” away from the SPAD surface. Figure 3-5 shows that this location is well within the free stream flow.

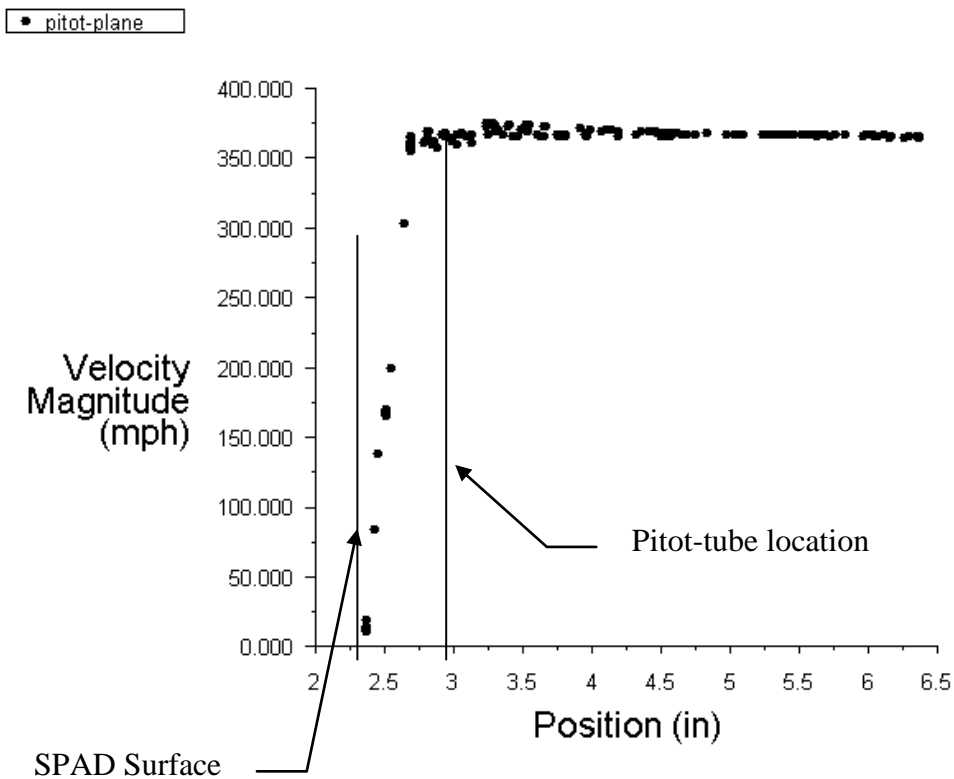


**Figure 3-5: Velocity Magnitude Profile Across the y-Direction from the SPAD Surface Outward in the Vicinity of the Pitot Tube**

### 3.3.3 Comparative Analysis

Finally, the SPAD hemispherical nose cone model was compared head to head with the SPAD blunt nose model. The blunt nose model removed all of the 2.364 radius curvature. A simple blunt nose was constructed to the minimal allowable height of 1.125 inches. Removing any sharp edges the outermost circumference was filleted with a 0.5 inch radius. Shown in Figure 3-6 on the following page, the SPAD blunt nose model was meshed identically to the SPAD hemispherical nose model to eliminate any discontinuities due to changes in mesh size and shape.



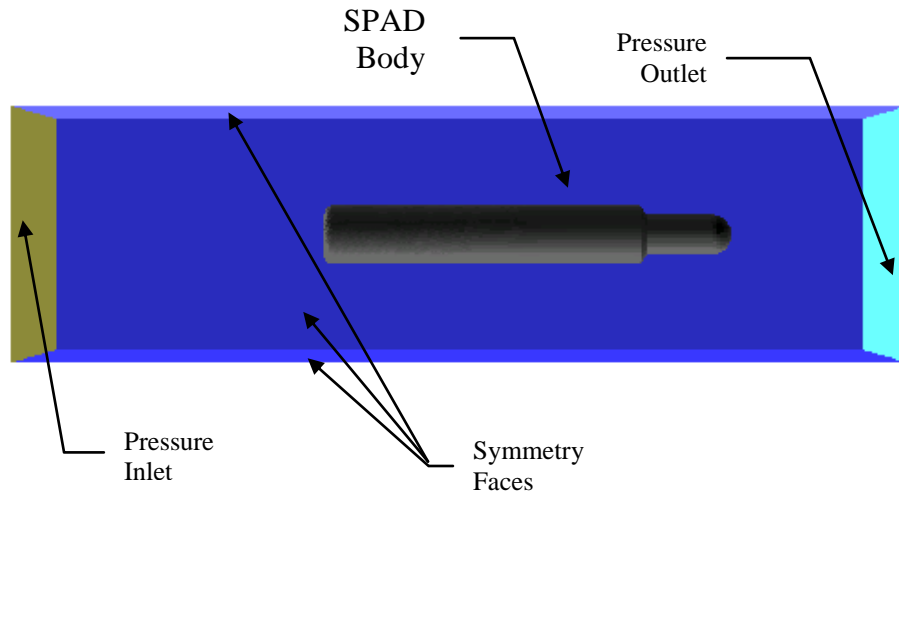


**Figure 3-6: GAMBIT Model of the Three-Dimensional SPAD Body with a Blunt Nose Cone**

The model was analyzed in an identical flow environment to the SPAD hemispherical nose cone model. The results are shown in Table 3-2 with the results compiled from the Maximum Velocity Analysis. When compared to the blunt nose model there is a clear need for a streamlined nose cone. The drag force from the blunt nose posts an increase of 300% over the hemispherical nose. As range is directly related to drag this increase in drag force alone would severely reduce the maximum range in the SPAD CONOPS (Raymer 2006). For this reason, a streamlined nose cone must be incorporated into the SPAD design. Simply leaving the nose as-is is not a viable option.

	<b>Lift (lbf)</b>	<b>Drag (lbf)</b>
<b>SPAD Hemispherical Model</b>	0.40	4.79
<b>SPAD Blunt Model</b>	0.35	14.37

**Table 3-2: Comparative Lift/Drag Data @ 350 mph**

---

## Chapter 4: Structural Analysis

---

After the aerodynamic analysis was completed, values regarding the loading of the nose cone were resolved. From this loading data, structural analyses were able to be completed to strengthen designs and prove their ability to resist these pressures. As each nose cone design is fundamentally different from each other, they can not all be analyzed by employing the same method. Tests have been selected in order to produce either comparable results or essential data for each design type. Much like CFD, computer assisted engineering software can use Finite Element Analysis (FEA) to provide numerical solutions to the mechanical environment. This allows for models to be analyzed as to their physical strengths and weaknesses in the virtual environment. As loads are introduced to a structure, FEA can calculate the resulting stresses and deformations. By inputting material properties for each specific model, FEA can accurately produce solutions providing necessary information about the design.

Three of the four designs were selected for a structural analysis. The design that was not selected was the foam nose. This was because the material properties could not accurately be analyzed in the FEA solver ANSYS, therefore the foam nose analysis was conducted in the experimentation phase. The three designs that were selected were the Spring-Loaded Nose, the Inflatable Nose and the Rubber Nose. The Spring-Loaded Nose is a rigid mechanical structure, so the benefits in using FEA compared to bench-top testing are clear. Internal stresses and deformation effects can easily be calculated using a numerical solver. The Inflatable Nose was not analyzed using FEA but simply the inside pressure was resolved. The Rubber Nose was analyzed using FEA to provide an initial design. Since the Rubber Nose is to be constructed out of a synthetic urethane

rubber, the specific material properties are unknown and the numerical solver only provided approximate solutions for deformation effects.

#### **4.1 Spring-Loaded Nose**

The aerodynamic analysis provided the loading distribution over the surface of the nose cone. A constant 2.5 psi pressure over the entire nose cone surface was used in the Spring-Loaded Nose cone analysis. A mission mode analysis was completed in order to prove the nose cone's viability as a design as well as a failure mode analysis to provide engineering margins of safety.

##### **4.1.1 Mission Mode**

For the mission specific variables such as  $p_{\max}$  and F1 load, maximum deformation and maximum equivalent stress have been evaluated via FEA. Acceptable maximum deformation has been arbitrarily defined at 0.005". Acceptable maximum equivalent stress has been arbitrarily defined at 2,175 psi which provides a factor of safety of two.

Sections were first analyzed in the flow environment where they are only affected by the flow pressures. This provided the necessary force information along the spring axis of the assembly to properly size the wave spring. A break down of the axial forces by section is shown in Table 4-1 on the following page. Only section two through section four exert a force on the spring as section one is supported directly by the base plate.

<b>Section</b>	<b><i>Axial Force (lbf)</i></b>
1	7.8542
2	9.8175
3	13.748
4	12.469
2-4	36.035
<i>Total Assembly</i>	43.7

***Table 4-1: Axial Force at  $p_{max}$***

From this data a wave spring must be able to exert at least 36.035 lbf at the F1 position. A spring was chosen to exert a 50 lbf. While the factor of safety is only 1.4 for the available spring force to the force at  $p_{max}$  an oversized spring would result in an unnecessarily highly loaded system.

Sections were then analyzed for deformation effects and equivalent stress in the flow when it would be affected by both the flow pressures as well as the force exerted by the load spring in the F1 position. Table 4-2 shows the material parameters used to complete FEA calculations.

Young's Modulus	2.9008x10 <sup>5</sup> psi
Poisson's Ratio	0.394
Density ( $\rho_{ABS}$ )	3.685x10 <sup>-2</sup> lbm/in <sup>3</sup>
Tensile Yield Strength ( $\sigma_{Y_{ABS}}$ )	4351 psi
Operating Temperature Range	-180°F to 220°F

***Table 4-2: Material Properties of ABS Plastic (ANSYS 2006)***

Finite element analysis of the Sections, Figure 4-1 to Figure 4-8, show an exaggerated representation with realistic numerical results of the distribution of both total deformation and equivalent stress present in the above scenario.

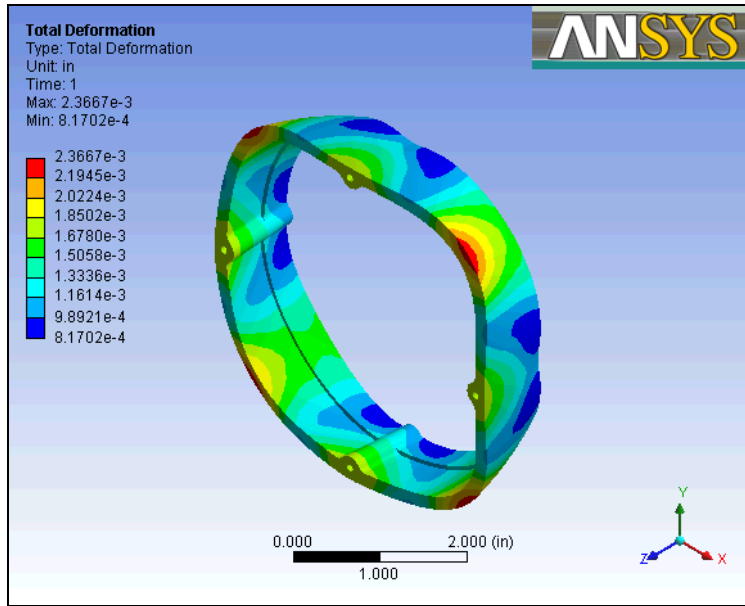


**Figure 4-1: Deformation Distribution @  $p_{max}$  & F1, Section1**

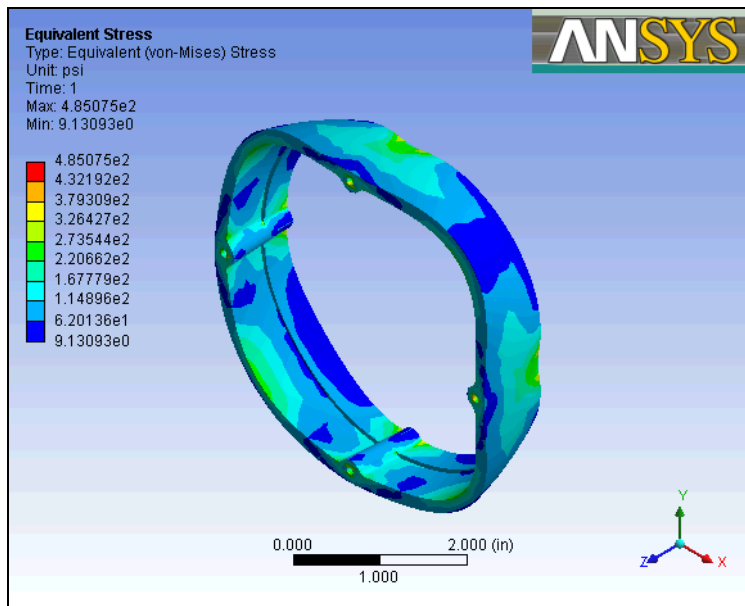


**Figure 4-2: Equivalent Stress Distribution @  $p_{max}$  and F1, Section one**

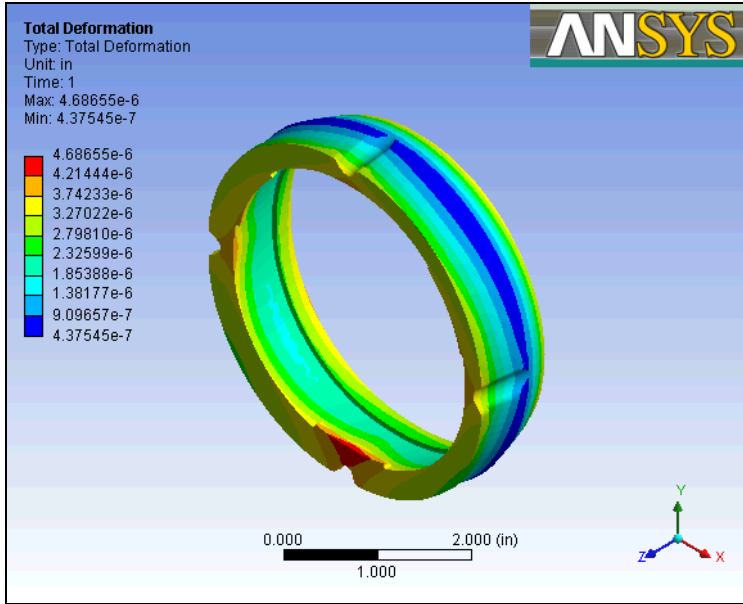


**Figure 4-3: Deformation Distribution @  $p_{max}$  and F1, Section two**

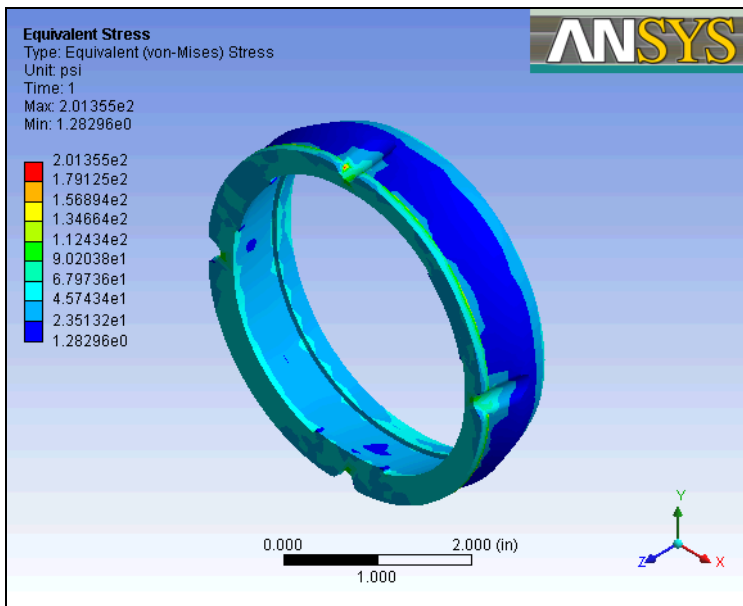


**Figure 4-4: Equivalent Stress Distribution @  $p_{max}$  and F1, Section two**

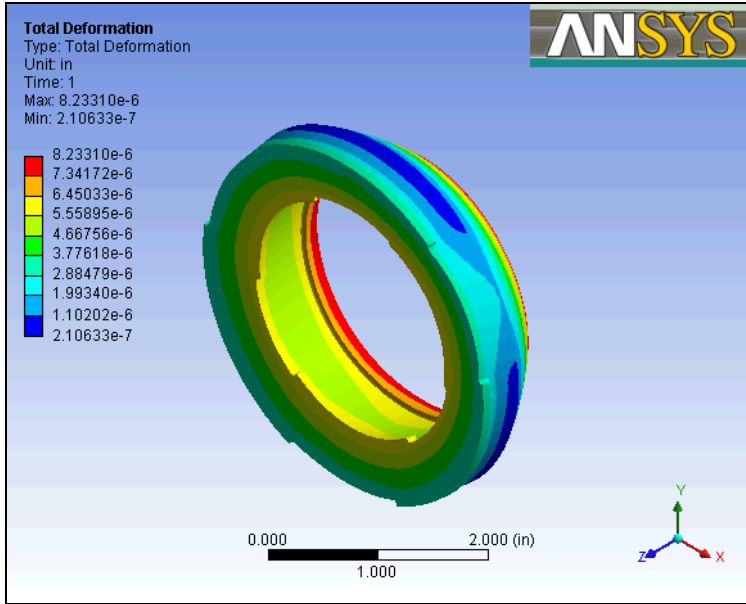


**Figure 4-5: Deformation Distribution @  $p_{max}$  and F2, Section three**

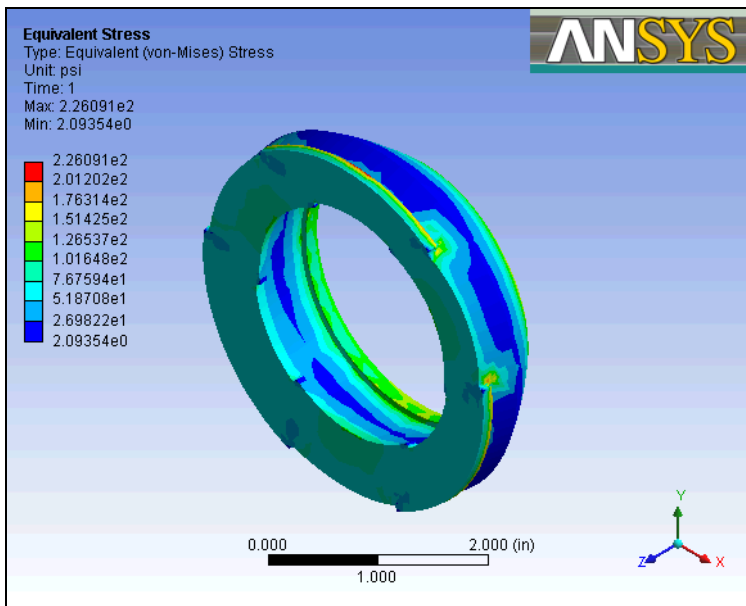


**Figure 4-6: Equivalent Stress Distribution @  $p_{max}$  and F1, Section three**

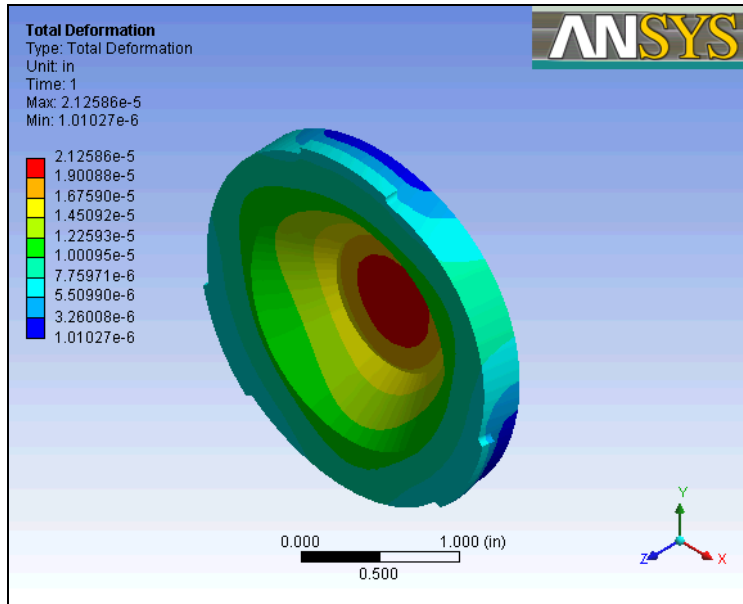


**Figure 4-7: Deformation Distribution @  $p_{max}$  and F1, Section four**

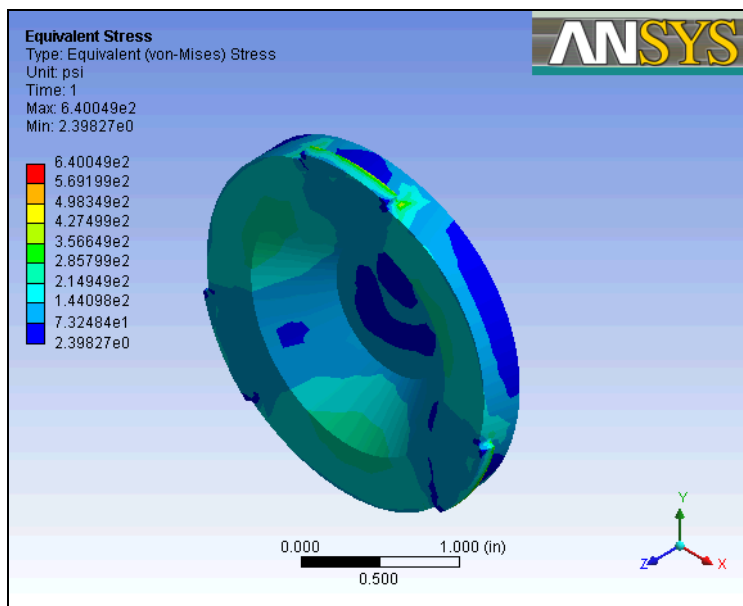


**Figure 4-8: Equivalent Stress Distribution @  $p_{max}$  and F1, Section four**

The base plate was analyzed using a different method. With a spring selected and defined as 50 lbs in the F1 position and with dynamic pressure having little to no effect on the base plate, analysis was completed to show total deformation and equivalent stress using only the spring force as a load.



Elastic Modulus	10.2 x 10 <sup>6</sup> psi
Poisson's Ratio	0.35
Density ( $\rho_{AA6061}$ )	0.0975 lbm/in <sup>3</sup>
Yield Strength ( $\sigma_{Y_{A6061}}$ )	40,000 psi
Operating Temperature Range	-180°F to 220°F

**Table 4-3: Material Properties, Aluminum A6061 (ANSYS 2006)**

The material properties used to complete analysis of the base plate section are shown in Table 4-3. For analysis, the load was applied over the area in which the spring end occupies. The supports, resisting the axial force, were positioned on the surface of each counter-bored screw hole. The results, shown in Figure 4-9 and Figure 4-10, conclude that the base plate section should be able to withstand the forces exerted on it for the duration of its mission as the deformation and equivalent stresses are below minimums.

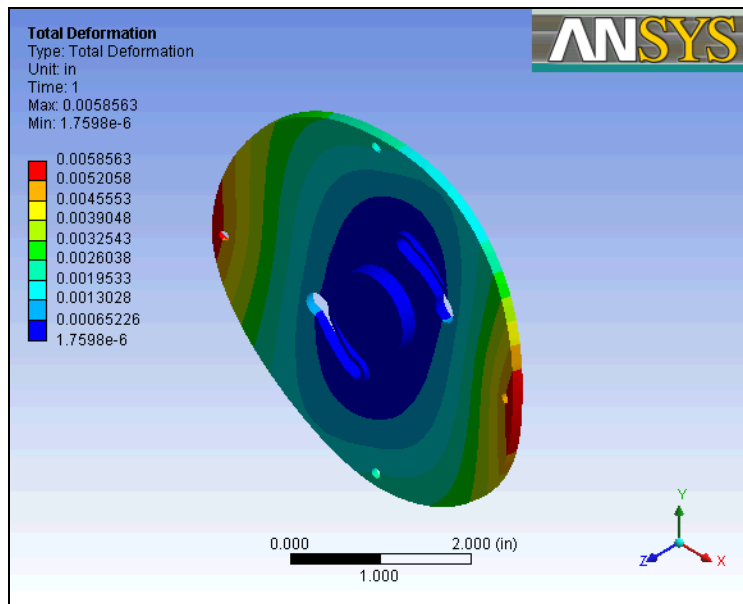


**Figure 4-9: Deformation Distribution @ F1. Base Plate**

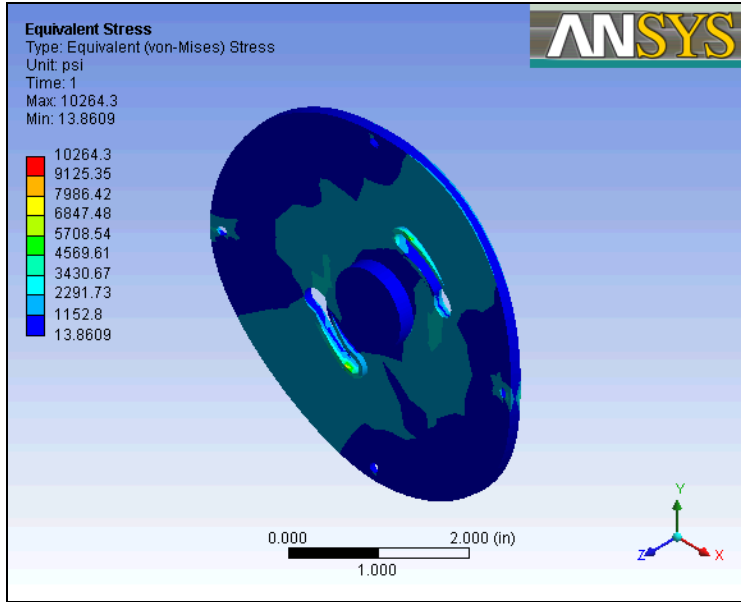
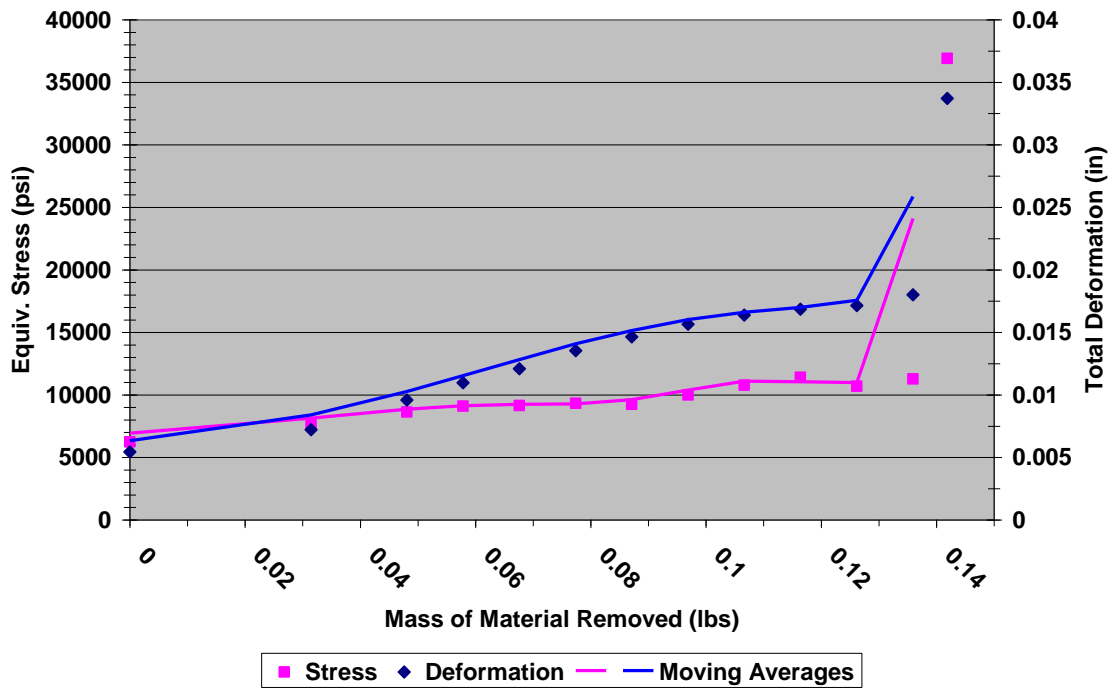


*Figure 4-10: Equivalent Stress Distribution @ F1, Base Plate*

#### **4.1.2 Weight Saving Tradeoff**

As stated in Section 2.1.6 the overall weight of the Spring-Loaded Nose is too heavy. 61% of this mass must be removed without sacrificing substantial strength. FEA was used to produce Material Removal vs. Strength Reduction curves in the form of deformation and stress increases. Using these curves a maximum amount of material was able to be removed from certain sections without compromising the structural integrity. Only sections 2-4 and the base plate underwent this optimization as there was no excess of material to remove from section 1. Figures showing the original and optimized geometries are shown in the appendix.

### Weight Saving Trade-off Study



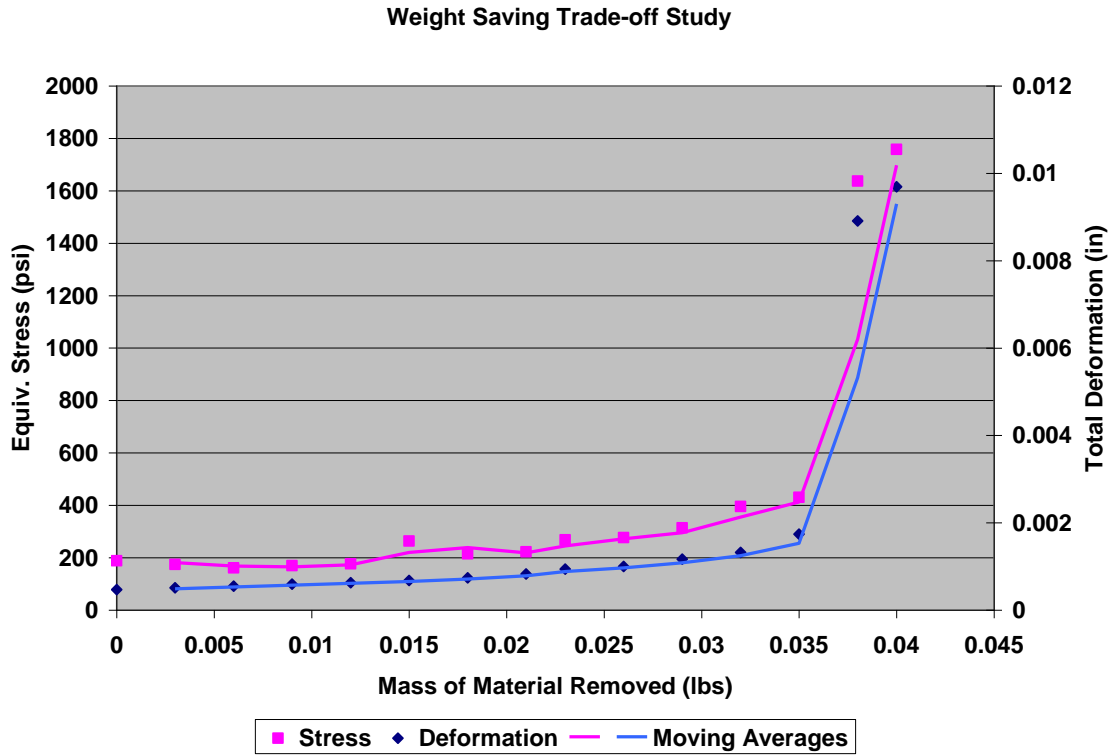
*Figure 4-11: Weight Saving Trade-off Study, Base Plate*

Figure 4-11 shows the above stated relationship between material removed from the base plate to the stress and deformation resultants. The data shows that as material is removed there is less area to distribute the force and both the stress and deformation increase. There is a period where material is continued to be removed and the stress and deformation seem to not increase by much. It is the high end of this period where the maximum amount of material removed is selected.

0.097 lbs was removed from the base plate section. That is a 43% reduction in part mass and an overall assembly mass reduction of 17%.

Continuing with the trade-off study, section two was analyzed second. Material was sequentially removed from the inside of the section. Sidewall thickness on the inside radius was kept at a

constant of 0.05” and only the depth was changed. Four areas, symmetric about the center axis, were where the material removal was focused.



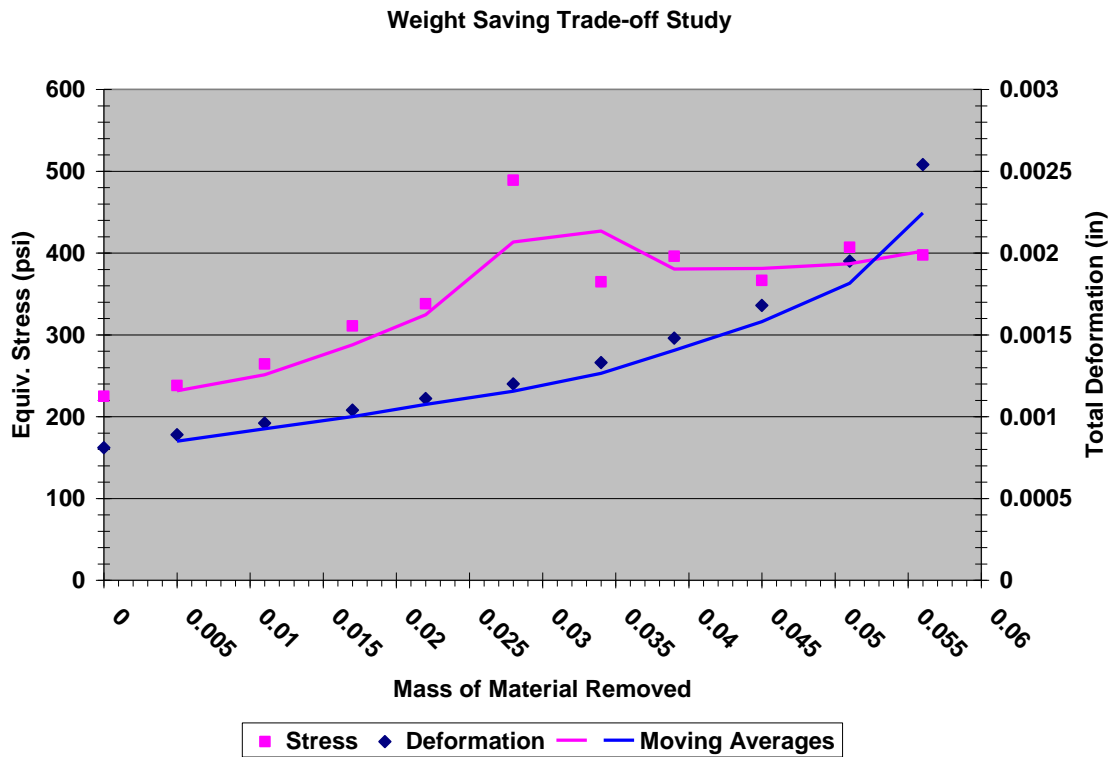
*Figure 4-12: Weight Saving Trade-off Study, Section two*

Figure 4-12 shows the weight saving relationship for section two. Results show that material removal has little to no effect on the overall strength of the section until 0.038 lbs of mass is removed. At this point the well dug into the section has pierced the face of the opposing side. Very quickly the section deforms under the newly created very high stress.

Creating a hole in the face of hemispherical face is not practical in the first place because of undesirable aerodynamic effects; however, the trade-off study has shown that it also has undesirable structural effects. Because of this, the depth of the well has been set at 0.55”, giving plenty of clearance for the front face. This removes 0.029 lbs of material from the section. That

is a 30% reduction in weight for the section and an overall 5% weight reduction for the assembly.

Section three also underwent a weight optimization. Similar to section two, material was removed from section three by the use of a well within the slide structure. However, since the outside radius was constant for this section one continuous area was able to be removed.



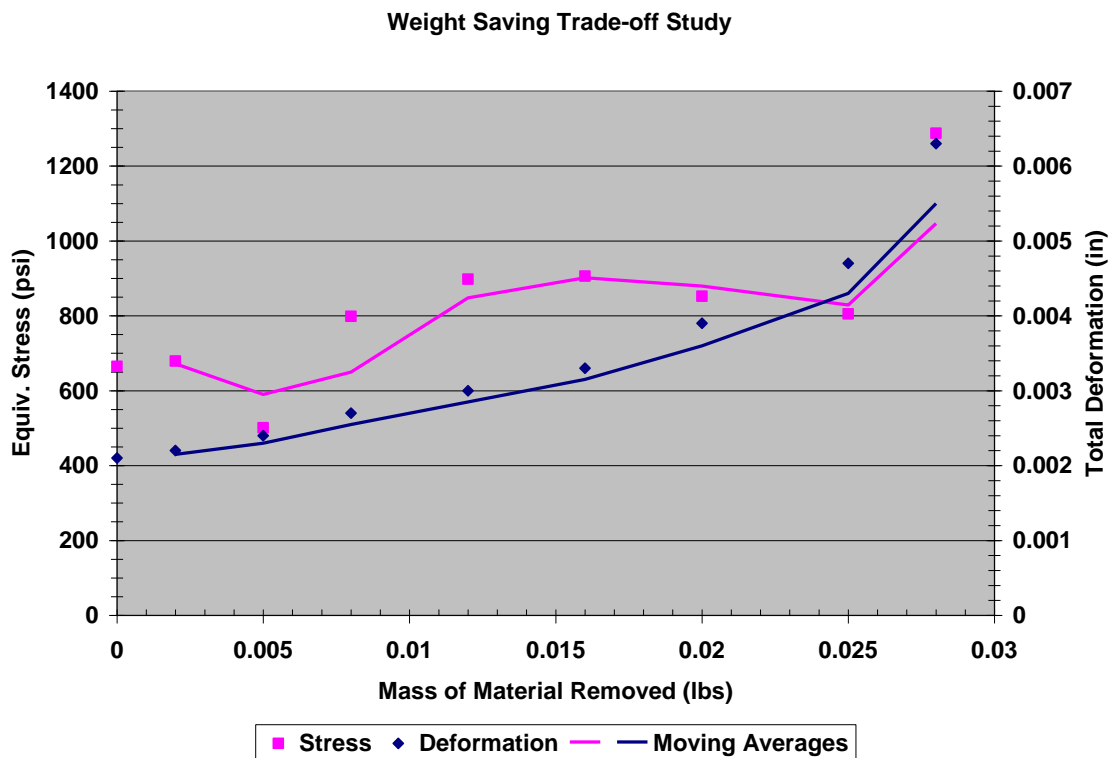
**Figure 4-13: Weight Saving Trade-off Study, Section three**

Figure 4-13 shows the trade-off study for section three. Much like the previous section two, as more material is removed from the slide portion of the section, the equivalent stress and total deformation increase. This figure however shows a bump in the stress plot at 0.028 lbs of material removed. At this point, enough material was removed to distribute the forces over less of an area but not enough material was removed to let the section warp. Because of this stiffness

and lack of material the stress plot spikes in this area. Ignoring this single effect, 0.045 lbs of material removed was selected as the ideal value of mass.

Removing 0.045 lbs from section three is a 36% reduction. Overall this optimization reduced the assembly mass by 8%.

The final section, section four, underwent an optimization as well. Being the smallest section there was less material to remove, but an trade-off study was conclude to remove whatever excess there was.



**Figure 4-14: Weight Saving Trade-off Study, Section four**

Following the similar patterns of the previous sections, the results from the mass optimization are shown in Figure 4-14. The results show an exponentially increasing total deformation while equivalent stresses slowly increase as well. A mass of 0.019 lbs was chosen to be removed. This

allowed for plenty of spring clearance, sidewall thickness as well as allowed for plenty of material along the front face.

A 0.019 lbs mass removal is a 28% mass reduction for the section as well as a 3% reduction for the entire assembly.

<b>Section</b>	<b>Original Weight (lbs)</b>	<b>Optimized Weight (lbs)</b>	<b>Percent Reduction</b>
Base Plate	0.223	0.126	43%
Section 1	0.066	-	0%
Section 2	0.096	0.067	30%
Section 3	0.125	0.080	36%
Section 4	0.069	0.050	28%
<b>Total</b>	<b>0.579</b>	<b>0.389</b>	<b>33%</b>

*Table 4-4: Summary of Weight Saving Optimization by Section*

Through this optimization a total of 33% of the mass was removed. The system can still support the required loads by not deforming significantly or failing. While the amount of material removed was not enough to meet the required total mass of 0.36 pounds, no more material could be removed without a complete redesign or possible failure of the structure.

#### **4.1.3 Failure Mode**

A failure mode analysis is a very simple way to improve a part design. Understanding at what loading, what circumstance and where a part fails provides information on how to make that specific part stronger, more durable and overall more useful to the system it is incorporated in. Failure mode analysis also provides resultant margins of safety in part designs. Each part within the Spring-Loaded Nose Cone assembly was evaluated using FEA to find failure points.

The first system to be analyzed was the screws that attach the base plate to section one. These screws are to hold the force exerted by the compression spring when fully extended so their

strength is critical to the assembly. 4-48 size screws are used Table 4-5 shows the screw parameters.

<b>#4-48 Screw</b>	
Effective Length	0.224”
Number of Threads per Inch	48
Major Diameter	0.112”
Number of Threads Engaged	10.8

**Table 4-5: #4-48 Screw Parameters (Oberg 2000)**

Equation 4-1 is used to find the thread stress area. This area is important because it is the distribution of the load applied by the screw across the area of the material being screwed into. A larger screw distributes a load across a larger area and thus decreases stresses (Hibbeler 2008).

$$A_{TS} = .7854 \left( D_M - \frac{.9743}{N_{TPI}} \right)^2$$

**Equation 4-1: Thread Stress Area (Oberg 2000)**

In this case, each screw needs to resist a minimum force of 12.5 lbf to counteract the spring. Acceptable minimums were set at 25 lbf, giving a designed factor of safety of 2. Using results from Equation 4-1, Equation 4-2 provides values for the force required to pull a screw from its threads.

$$F_{PO} = \sigma A_{TS} N_{ET}$$

**Equation 4-2: Pull-Out Force per Screw (Oberg 2000)**

Given the parameters for a #4-48 screw and the material properties of ABS plastic, the thread stress area was found to be  $6.605 \times 10^{-3} \text{ in}^2$  leading to a screw pull-out force of 309 lbf. The margin of safety provided by this screw design is 12.4.

The next failure analysis was directed at each individual section. FEA provides values illustrating at what loading the sections would fail. Individual analyses were completed by



applying increasing loads on the contact point where the spring force is applied as well as increasing pressures on the outside surface geometry until failure. Table 4-6 shows the results of these analyses.

Section	Force to Yield (lbf)	Force to Deformation (lbf)	Pressure to Deformation (psi)
1	560	275	23
2	900	600	55
3	625	450	90
4	375	200	70
Base Plate	430		-

*Table 4-6: Spring-Loaded Nose Failure Mode Analysis Results*

## 4.2 Inflatable Nose

The Inflatable Nose is not a rigid structure like the Spring-Loaded Nose. It is because of this fact that it was not analyzed in the same fashion. The preliminary structural analysis of this nose cone design was a simple proof of concept. As the design relied heavily on the use of off-the-shelf components, the 12g CO<sub>2</sub> cartridge was an integral part to the design. Therefore, the viability of this component was analyzed.

The volume of CO<sub>2</sub> gas compressed in a 12g cartridge is a fixed value. Thus, when released all of this volume is transferred to the inflatable structure. Pressures outside the inflatable reach 2.5 psi, so the internal must be in moderate excess of this value. However, internal pressures can not be too high as there would be a risk of blow out. Boyle's Law states that  $P_1V_1 = P_2V_2$ , so the following formula, Figure 4-3 on the following page, provides the pressure supplied to the inflatable chamber after inflation.

$$P_i = \frac{4200}{V_c}$$

***Equation 4-3: Relationship between Pressure Inside of the Inflatable to the Volume Inside the Inflatable due to a 12g CO<sub>2</sub> Cartridge***

The solution to Equation 4-3 results in a 152 psi internal pressure, well exceeding the 2.5 psi pressure on the outside geometry. This pressure is simply too high. A typical car tire pressure is only 32 psi. As the volume inside the nose cone is a fixed value, the compressed volume of the CO<sub>2</sub> cartridge must decrease for this concept to progress in design.

### **4.3 Rubber Nose**

The Rubber Nose was the second model evaluated in the numerical solver. It was understood from the conceptual phase that different types of rubber exhibit different material properties. As there are various types of rubber, natural, vulcanized, urethane or silicone, the preliminary CAE analysis was used to simply provide an approximation for the rubber nose cone geometry. As it would have been expensive and time intensive to simply fabricate and test multiple nose cones all with differing geometries, the approximate structural responses predicted in the solver provided an element of speed of production that was needed.

Elastic Modulus	884.73 psi
Poisson's Ratio	0.49
Density	3.613x10 <sup>-2</sup> lbm/in <sup>3</sup>
Tensile Yield Strength	1,339.7 psi

***Table 4-7: Material Properties: Natural Rubber (ANSYS 2006)***

In order to simplify the analysis the back was removed from the structure and just the nose cone model alone was imported into the solver. A rubber material, shown in Table 4-7 and listed in the ANSYS database, was selected for the material properties to be imported into the solver.

While it was known that the material properties of this rubber would not be exactly the same as the materials used in the fabrication stage it provided a general solution. A thick tip and base structure were incorporated to produce different compressive effects. The thickness of the nose cone side-wall was successively changed until results were as desired. It was found that adding a reinforced circular mass in the front of the nose cone resulted in a very symmetrical compression under applied operational loading. It was also found that building up mass from the base to a certain height of the rubber nose encouraged the buckling at certain position. ANSYS predicted that a 0.1 inch thick sidewall would produce the proper deformation and buckling effects in the rubber nose.

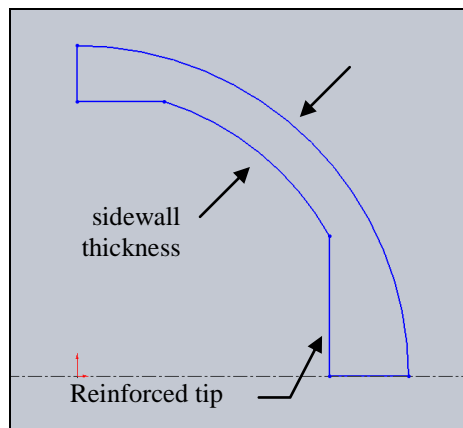


**Figure 4-15: Rubber Nose Cone Model Cross-Section**

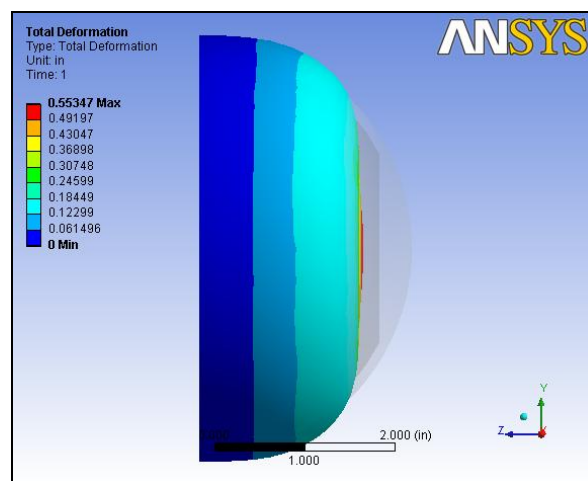


**Figure 4-16: ANSYS Predicted Compression of Rubber Nose @ 40 lbs**

---

## **Chapter 5: Fabrication and Experimentation**

---

In order to form a more complete analysis of the nose cone designs there was a fabrication and experimentation phase. This allowed for designs to be physically tested in the bench-top environment as to their reactions to load forces and/or conformity to numerical predictions. The spring-loaded cone was not one of these candidates. Due to time constraints and cost of production, a spring-loaded nose cone was not a candidate for bench-top testing as the FEA performed in Chapter 6 provided sufficient results. The inflatable nose was also not fabricated. It was found that the excess of internal pressure and the shear complexity of the design hampered the ability to construct a prototype model. The two remaining designs, the rubber nose and the foam nose, were the two models that were fabricated. Since the conceptual phase it was known that the specific material properties of solid rubber and foam rubber were variables that needed to be solved. The fabrication and experimentation phase allowed for these last two designs to be thoroughly analyzed.

### **5.1 Fabrication**

The rubber nose and the foam nose were constructed using similar methods. First a mold of the outside surface of the nose cone was constructed. Shown in Figure 5-1 on the following page, the base model contained the outside geometry of the nose cone at a 2.364" radius.

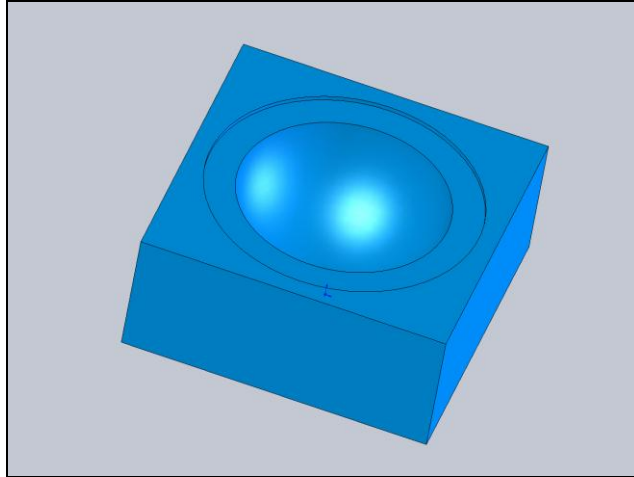


**Figure 5-1: Model of the Foam/Rubber Nose Cone Base Mold**

While the foam nose was to be a solid hemispherical piece of foam, the rubber nose was designed to be hollow. This meant that an insert would have to be placed within the model after the rubber was poured in to create the proper geometry. Shown in Figure 5-2, the mold insert has a blunt nose, followed by a curvature and then a flat section. This shape produced the thick tip, constant sidewall thickness and reinforced base section of the Rubber Nose design.

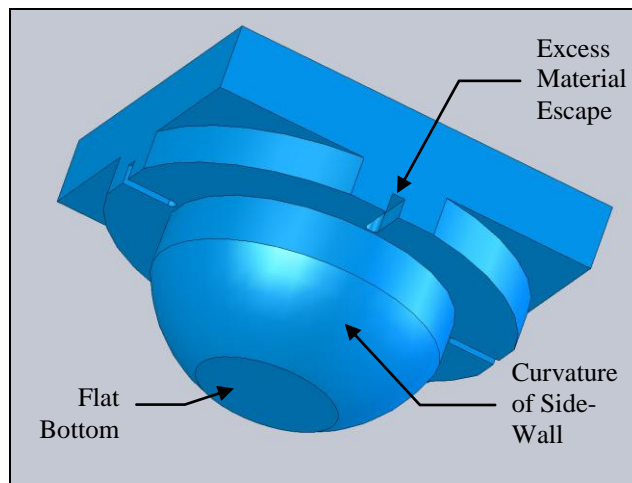


**Figure 5-2: Model of the Rubber Nose Cone Mold Insert**

### **5.1.1 Materials and Methods**

The materials selected for the Foam Nose and the Rubber Nose were Smooth-On's urethane lines in Flex-Foam, Vyta-Flex and PMC series. Flex-Foam was used for the foam nose. Vyta-Flex and

PMC were used for the rubber nose. As each of these products are not marketed by publicizing material properties such as elastic modulus or Poisson's ratio but instead present hardness, density and elongation at break; two foams and three rubbers were chosen to test out in the lab environment. Each of these materials are shown in Table 5-1.

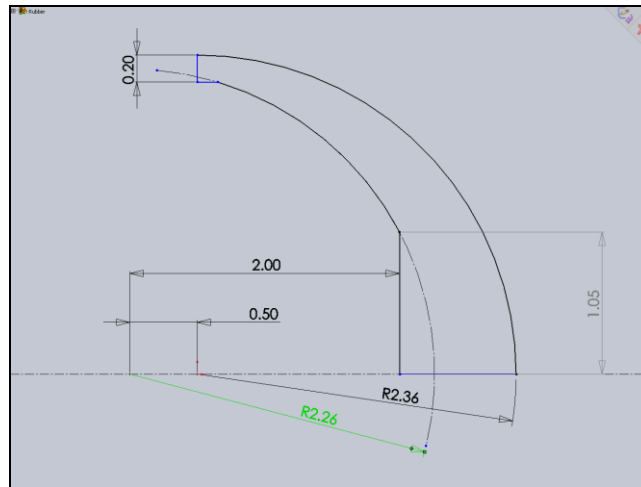
	Density (in <sup>3</sup> /lb)	Hardness (Shore A)	Elongation at Break
<b>FlexFoam V</b>	275-300	-	-
<b>FlexFoam X</b>	150-200	-	-
<b>VytaFlex 50</b>	-	50A	400%
<b>VytaFlex 60</b>	-	60A	480%
<b>PMC-780</b>	-	80A	700%

***Table 5-1: Material Properties of Smooth-On Products (Reynolds Advanced Materials 2008)***

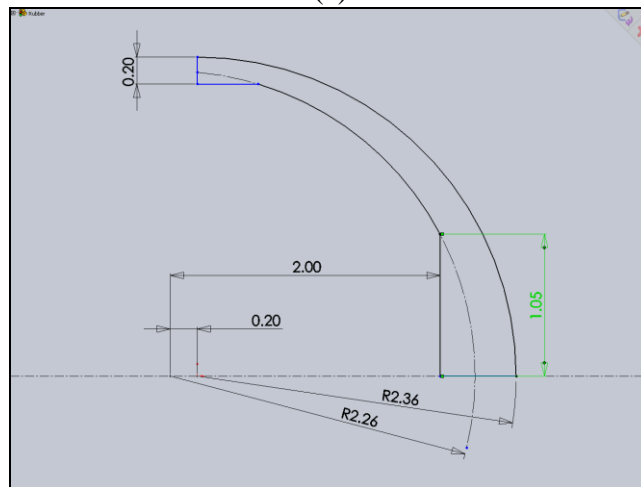
Each urethane nose was fabricated. The foam material was simply poured into the mold of the outer geometry. The rubber material was poured into the base mold and the insert was placed inside. After the published cure time had elapsed each nose was removed from the mold. As prematurely testing the molded parts can yield inconsistent material properties cure time was strictly adhered to.

It was very quickly found that the ANSYS prediction for the geometry of the rubber nose was incorrect. This was due to the generalization assumed in Chapter 4: that each urethane rubber would have similar material properties to natural rubber. A 1" thick sidewall produced a very weak structure and it was obvious that this structure would not be able to withstand the pressures encountered in flight. As the nose cone molds had already been fabricated and time was of the essence, new molds could not be produced. For this reason a simple solution was employed. Since the mold insert produced the tip thickness and sidewalls for the rubber nose, it was elected that simply lifting the insert out of the base mold with the curing rubber inside would produce thicker sidewalls. While this method created a variable sidewall thickness and a much thicker tip

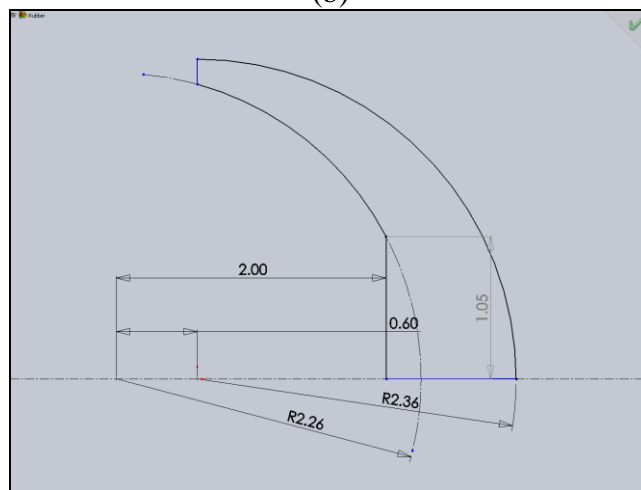
it produced much a stronger structure. Four different rubber noses were fabricated in this manner. Figure 5-3 shows their geometries.



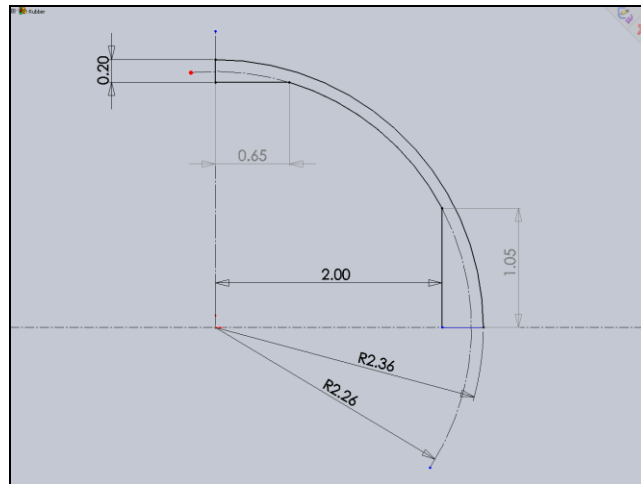
(a)



(b)



(c)



(d)

**Figure 5-3: Cross-Section Sketches for Each Rubber Nose Fabricated. (a) The VytaFlex 50 lifted 0.5" (b) The VytaFlex60 lifted 0.2" (c) The VytaFlex60 lifted 0.6" and (d) The PMC-780 with no lift.**

## 5.2 Experimentation

Once the rubber nose and foam nose models were finished curing, there were two foam and four rubber noses to test in the lab environment. The foam nose analyses focused on the ability of the foam to rebound after a state of compressed storage as well as the ability to retain original geometry under loads. The rubber nose analyses focused on increasing the accuracy of the results produced using ANSYS in the ability to resist deformation under loading and the designed ability to buckle. This was in order to produce the final rubber nose design, able to withstand the pressures of flight and forces for storage, to be fabricated and tested.

### 5.2.1 Foam Nose

The foam in the Foam Nose is comprised of many open cell urethane foam pockets. It is the material nature of these foam pockets to compress and stretch; the operation of the foam nose is based on this fact. However, this random structuring also causes foam to randomly fail. When compressed this causes an inability to rebound to an original geometry. Severe inability to rebound would render a foam nose useless as a viable option as a nose cone. In order to test the



ability of the foam to rebound under compressive forces compression set testing was undertaken. Compression set testing compares the original geometry of the foam to the post-compressed geometry of the foam. This yields a compression set value in the form of a percentage. Compression testing was also employed to resolve the force versus deflection curves for each foam density. FEA was not conducted with the Foam Nose due to the fact that after an exhaustive search no procedure was found in order accurately model the hyperelastic responses of foam.

#### 5.2.1.1 Experimental Procedure

Figure 5-4 shows the apparatus used in the compression set testing of the foam. The four screws provided the ability to uniformly compress each foam nose cone to a desired compressed length. A height of 1.125", the available area provided by the SLT, was used as the hold height for the rebound tests.

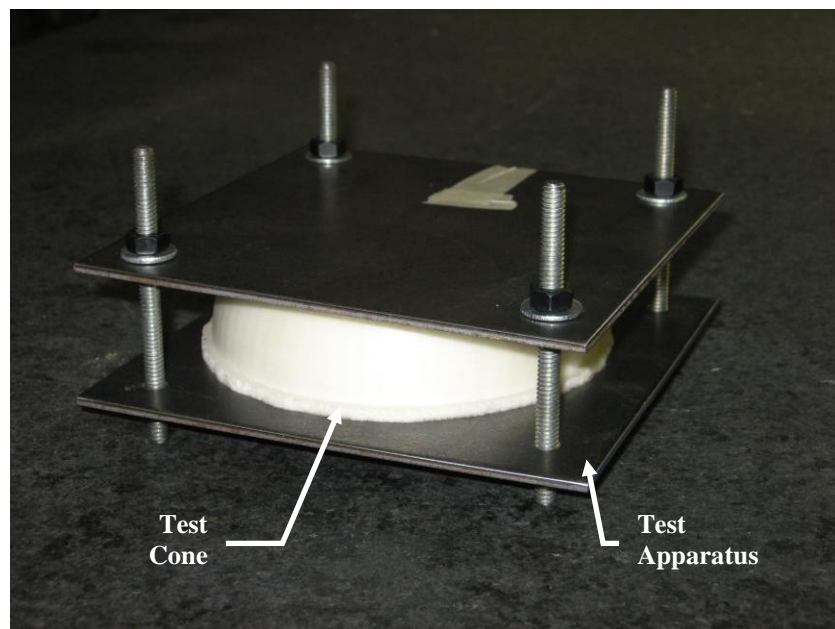


**Figure 5-4: Foam Compression Set Testing Apparatus**

Compression set testing was conducted in order to resolve time to rebound and completeness of rebound. As there is a projected five year shelf life in which the nose cone would be required to

be held in its compressed state viability of design for this period of time must be confirmed. The nose cone must rebound to the designed geometry within the short period of time when SPAD is ejected from the SLT. The compression set tests were conducted at two separate temperatures to also test the operational temperature range of the foam. The first test was conducted with the foam held overnight at 70°F. The foam was then released from the test apparatus and the rebound height was measured at 20 second increments. This method was duplicated after holding the foam over night at 0°F.

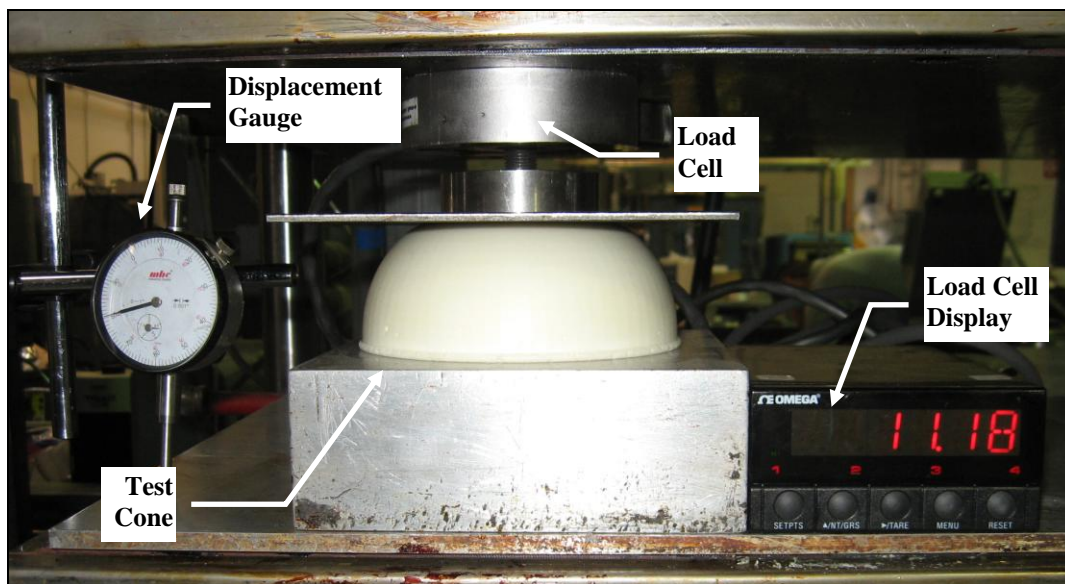


*Figure 5-5: Foam Vertical Compression Test Apparatus*

The force to deflection curves were resolved by employing a different method. Forces were applied to the nose cone along its center axis and deformation was measured at particular weight increments. Figure 5-5 shows the test apparatus. A *Carver 2'x2' Laboratory Press* was used to apply the vertical loading. An *Omegadyne, Inc. LCHD-3K* load cell, rated from 0-3,000 lbs, was used to measure the applied load. Vertical displacement measurements were displayed on the *MHC Industrial Supply* gauge.

### 5.2.1.2 Results

The compression set testing for the foam noses yielded the foam rebound curves shown in Figure 5-6.

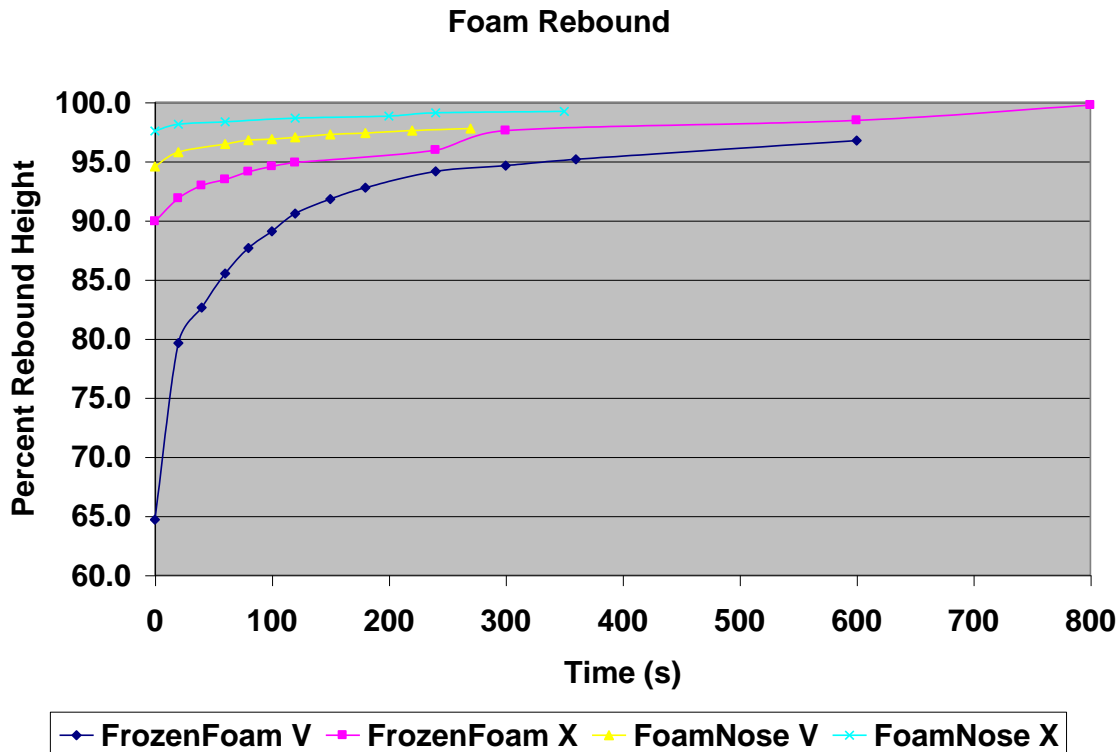
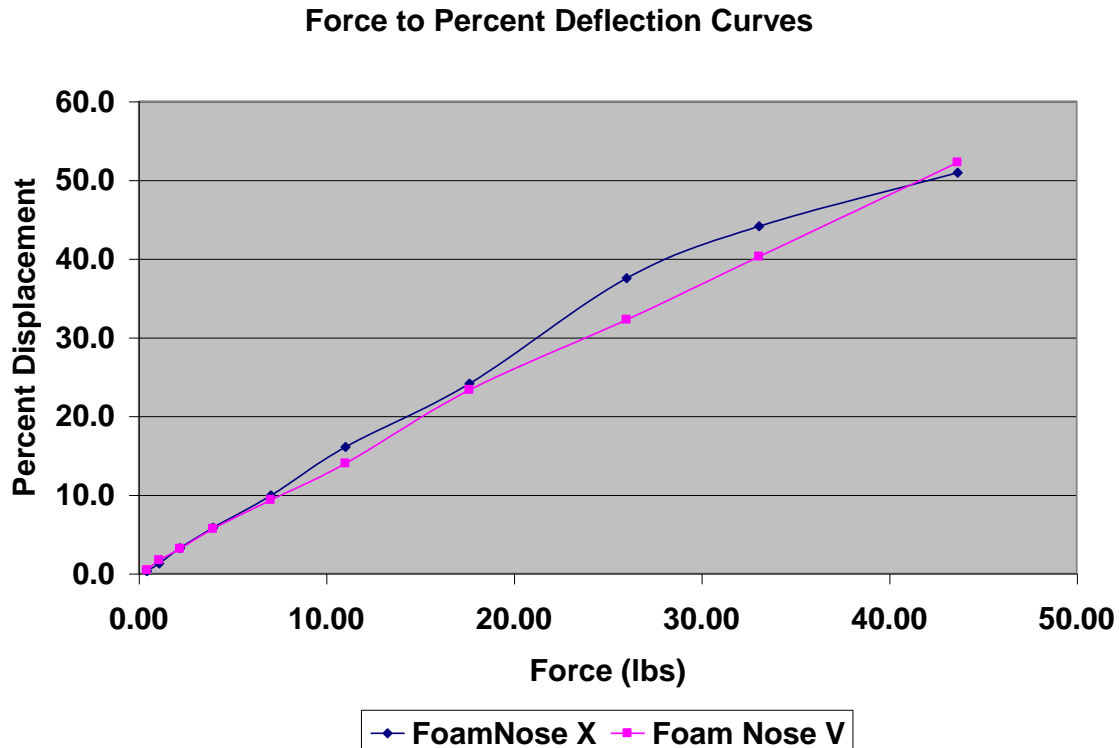


Figure 5-6: Time to Rebound of Frozen and Room Temperature Foams

Both the frozen and room temperature foams recover at least 95% of their original height by 6 minutes of elapsed time. As can be seen in the figure, the frozen foams took longer to rebound than their room temperature models. This can partly be attributed to the moisture, held within the open cell structures of the foam, freezing and holding the foam in its compressed state. While the room temperature foam exhibited an almost full rebound instantly, the foam could not be used successfully within the lower temperature ranges of operation as the rebound time is substantially long.

The force to deflection curves are shown in Figure 5-7. At 40lbs, the approximate flight loading, the foam height was compressed to 50% of its original dimension



*Figure 5-7: Force to Deflection Curve for Foam Noses*

This means that foam with a greater density must be used in order to resist deformation when flight loads are applied.

### 5.2.2 Rubber Nose

The rubber nose cones were analyzed in the bench-top environment. Unlike the foam noses, the rubber noses were examined physically in conjunction with FEA. Since the concept of the rubber nose was introduced it was known that the unknown specific material properties of synthetic urethane rubbers used in this application would yield physical results inconsistent to the FEA results of natural rubber. For this reason, these analyses attempted to improve the accuracy of the FEA model in order to aid in the production of the final rubber nose geometry.

### 5.2.2.1 Experimental Procedures

The analysis performed in Section 4.3 yielded results inconsistent with the physical model from section 5.1.1. These inconsistencies were due to the fact that the natural rubber was the material used to model the deformation effects of the urethane rubber noses. While it was assumed these two different materials would have similar material properties, that assumption was proven wrong in the fabrication stage. It was because of this that the first priority in the bench-top testing of the rubber nose was to improve the FEA model to accurately produce results for deformation effects concurrent with those of the physical tests. This was carried out by first bench-testing the five rubber nose cones in controlled tests. These tests produced force to deflection curves. Shown in Figure 5-8 is the test apparatus. Loads were applied by the *Carver 2'x2' Laboratory Press*. An *Omegadyne, Inc. LCHD-3K load cell* provided the force measurements while a *MHC Industrial Supply* gauge measured the displacement.

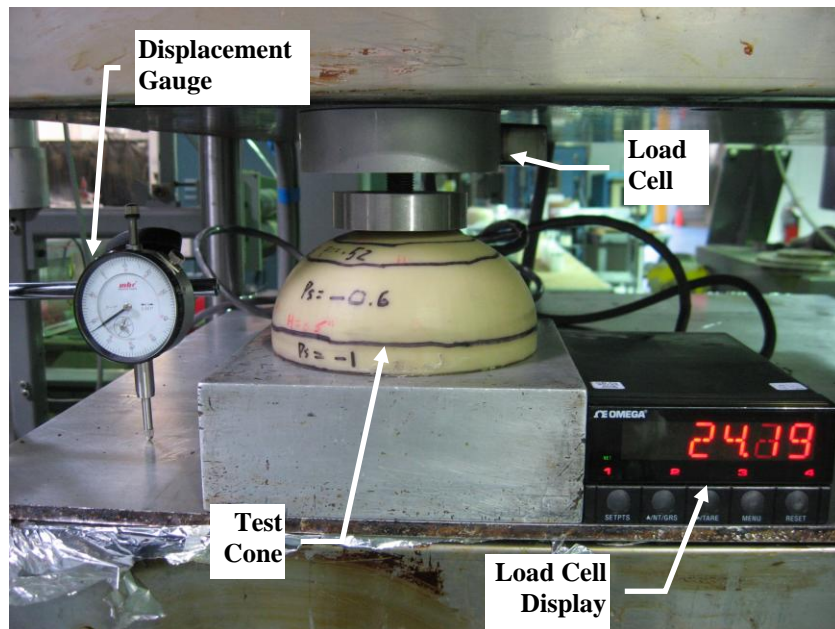


**Figure 5-8: Vertical Compression Test Apparatus**

This provided a similar and measurable loading environment to the numerical model resulting in a similarly measured displacement result. Force measurements were recorded in a table for every

0.1” of deformation. This data was then used to properly model each material in ANSYS. A comparable environment was created within the virtual model in which loads were applied over a controlled area 1” in radius to the top of the nose cone. The material properties were changed in accordance with a material datasheet found for urethane materials of 50A, 60A and 80A hardness shown in Table 5-2.

Shore A Hardness	Modulus of Elasticity (psi)
50A	100
60A	300
80A	1000

***Table 5-2: Material Properties of Urethane Rubber (Harkness Industries 2006)***

At each force recorded from the bench-top test, the numerically solved deformation was compared with the physical test. With the addition of the material properties of each specific type of urethane rubber nose, the ANSYS model accurately represented the physically recorded deformation.

The first analysis provided ANSYS with the required data to make its FEA solutions accurate. The second analysis used this, now correct, solver to design the ideal geometry for the rubber nose cone. The original design method was modified to fit the new rubber nose shape. Variables were attached to the sidewall thickness, base height and tip thickness. Changing the values of each of these resulted in very different effects. Increasing the size of the tip feature created a larger area that did not buckle and held rigidity. Increasing the height of the thicker base raised the height of the point at which the structure buckles. Modifying a combination of these variables produced a numerical solution to the rubber nose cone structure that buckled when 50 lbs was applied in a manner that was not disturbed the SLT geometry.

### 5.2.2.2 Results

The bench-top compression tests yielded results for a compressive force versus deformation curve. Each nose cone yielded very different results. This can be attributed to the varying nose cone geometries as well as the material properties of the different urethanes. These results are shown in Figure 5-9. The data shows that the PMC-780 is the ideal material for the rubber nose cone as it holds rigidity up to about 50 lbs where it then fails structurally and collapses. This is ideal as the structure can remain rigid for flight and then compress for storage at a minimal force of 50 lbs applied to the tip.

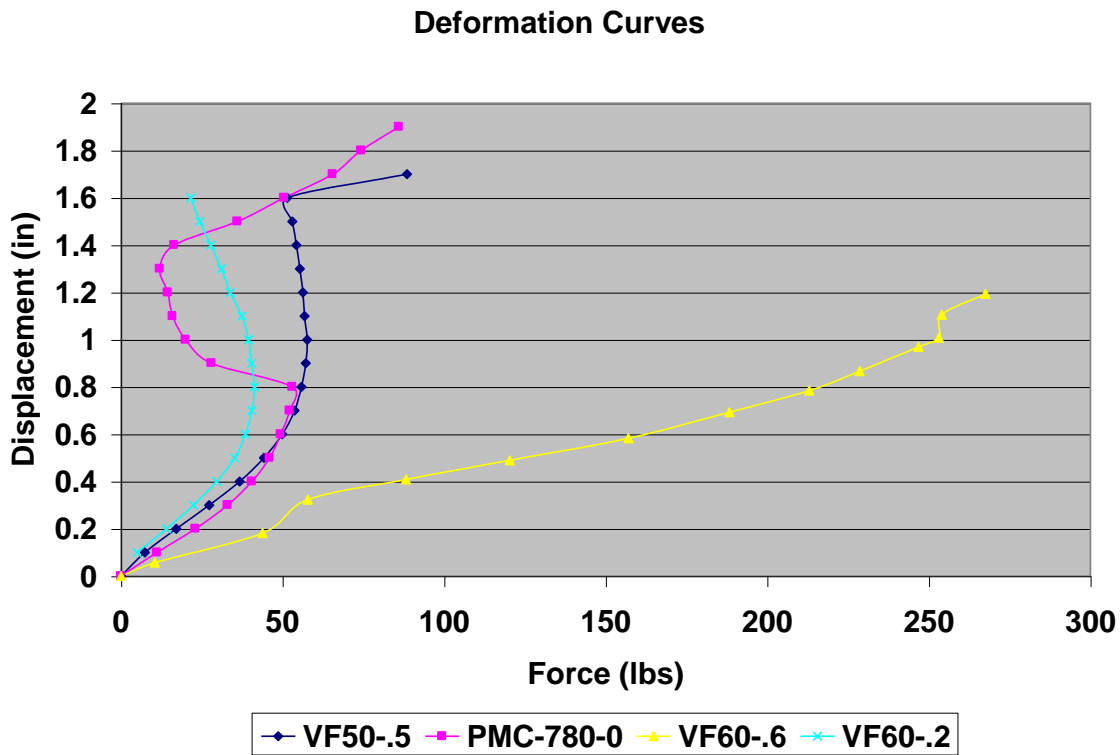


*Figure 5-9: Force to Deform Curves for Each Rubber Nose Cone*

The next best nose cone designs are the VytaFlex 50 lifted 0.5” and the VytaFlex 60 lifted 0.2”. Each of these nose cones held geometry up to about 45 and 55 lbs respectively and then failed structurally. The VytaFlex 60 lifted 0.6” is the clear underperformer of this test by holding structural strength indefinitely. While the ability to not deform significantly is a requirement, the

results for the VytaFlex 60 lifted 0.6” are undesirable as a nose cone that does not deform could not pack within the available geometry of the SLT. Deformations only occur in this nose cone through material, not structural, deformation. Through the results shown in the previous figure alone it would appear that the ideal material is the PMC-780 nose cone. However, it was found at removal from the test apparatus that the nose cone material had failed. Shown in Figure 5-10 are the spider cracks that formed as a result of the compression test. While it was published that this material had the ability to elongate to 700% its original length before failing, it is clear that the PMC-780 cannot be considered a possible material to be used in the nose cone design for its high risk of material failure.



***Figure 5-10: Failure of the PMC-780 Rubber Nose Cone***

For the above reason, the next best performing material, VytaFlex 60, was selected as the material to construct the final rubber nose from. Shown in Figure 5-11 on the following page is the ANSYS model next to the bench-top model for the VytaFlex 60 urethane nose. After the incorporation of the correct material properties for 60A hardness urethane rubber into the numerical solution, numerically predicted results correlated with physical test results. When



loaded with approximately 40 lbs the physical model deflected 0.700" while the ANSYS model deflected 0.730". As these two methods produced the same result it was decided that the numerical model was now correct in its solution.

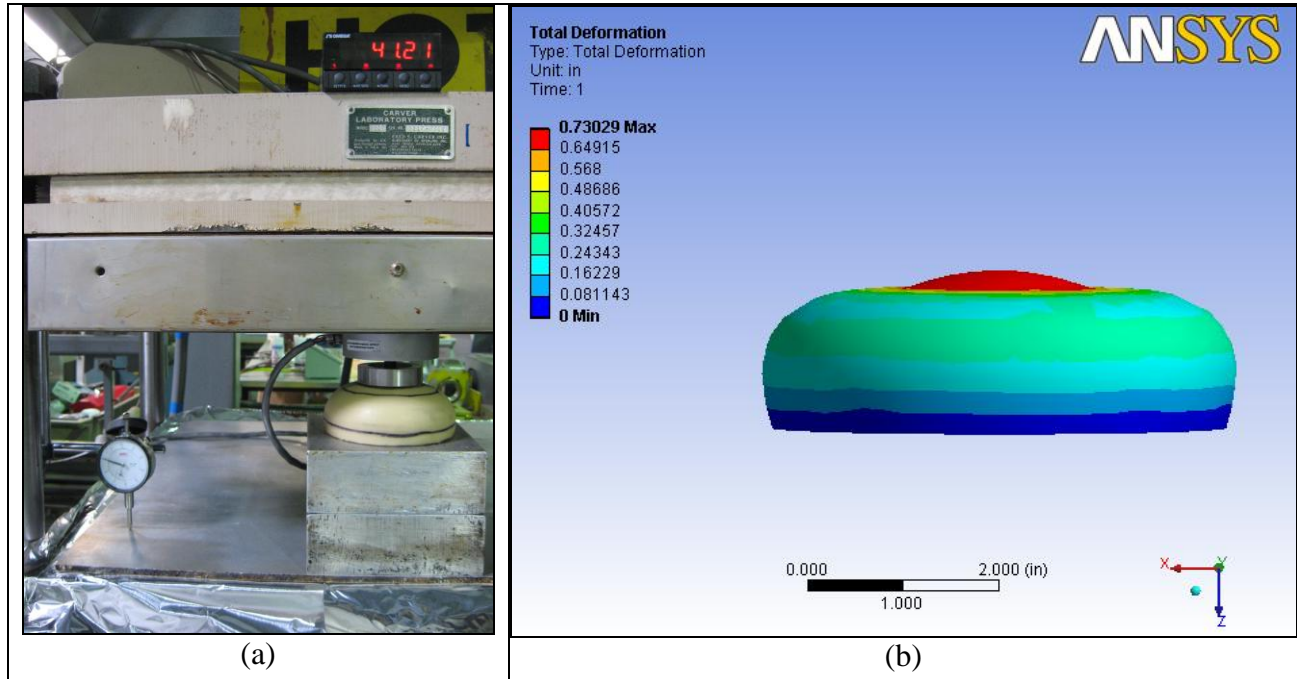


**Figure 5-11:** (a) The physical model is subjected to a 41.21 lbf load and deforms 0.700". (b) The ANSYS model is subjected to a 40.00 lbf load and deforms 0.730"

Once the numerical model was producing proper solutions, rubber nose cones of differing geometry were able to be examined in ANSYS for their reactions to loading. The end product of this method produced a nose cone whose geometry is shown in Figure 5-12.

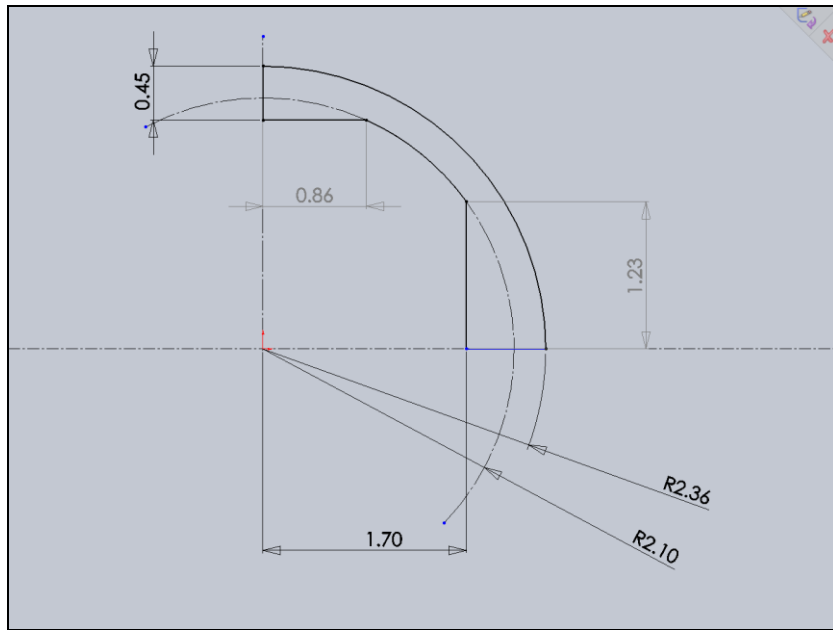


**Figure 5-12: Sketch of Finalized Rubber Nose Geometry**

Values were resolved through numerical analysis. The increase in material at the base to a height of 0.86" provided the location of the buckle to not push rubber material out in the radial direction but in the axial direction. This was so the nose cone would not get stuck within the limited radius provided by the SLT. The thickened tip provided a uniform collapse. A 1.23" radius nose tip was chosen for strength purposes; any greater of a radius and the nose cone would not buckle at the designed load of 50 lbs, any smaller radius resulted in the buckle to form at a loading below 50 lbs.

---

## Chapter 6: Summary and Recommendations

---

The aim of this qualifying project was to create a viable design for the nose cone of the SPAD vehicle. Mission requirements dictate that the nose cone be compressed while in an extended state of storage and then extend for the flight phase. Four fundamentally separate designs were conceptualized for the purpose of eliminating poor concepts and strengthening strong concepts. The concepts considered were: 1) the spring loaded nose; 2) inflatable nose; 3) rubber nose; and 4) foam nose. Extensive testing was performed on each design concept. Each method of analysis emphasized the comparable strengths and weaknesses of the four nose cone designs. Though the scope of the project was limited from the beginning by the 10-week time constraint, during this period of time, intensive design, fabrication and analyses took place. Despite the best efforts put forth, several aspects of the four designs remain untested and underdeveloped. This section will comment on a few of these areas and make recommendations to proceed.

### 6.1 Spring-Loaded Nose Cone

The Spring-Loaded Nose Cone design concept was to create a rigid structure that could fit the required geometry while in flight and then collapse in on itself for storage. The structure of this device was intensely analyzed within ANSYS. These analyses showed that the spring-loaded nose could withstand the pressures of the flight environment very well and collapse to fit within the required area. However, a prototype model was not constructed due to the time constraints. Stereolithography (SLA) was evaluated as a method of construction. SLA could produce accurate ABS prototype models. In order to fully examine the spring-loaded design, a prototype must be made to prove that there are no undesirable effects contained within the sliding mechanism.

## **6.2 Inflatable Nose**

The design of the inflatable nose was based on two main goals. The first was the creation of a zero-stress storage environment. The second was that the components would be, for the most part, off-the-shelf and readily purchased from distributors. While the design seemed complex, prior proof was found of the pressure bottle piecing mechanism as well as the pressure switch. The main drawback to this design was that the pressure bottle simply contained too much pressure. A smaller volume pressure bottle that provides the proper pressure within the nose chamber is needed to make the inflatable nose a potential candidate for application on the SPAD. After a search for a smaller volume pressure bottle, no solution could be found and any attempt to further the inflatable nose design was disbanded.

## **6.3 Rubber Nose**

The Rubber Nose design concept was to create a ductile structure that could retain a designed geometry for flight and then collapse for storage. The design was exhaustively tested for its compression and rebounding capabilities. It was found that the structure responded very well when flight loads were applied. It was also found that the forces required to pack the rubber nose were very desirable. However, all these tests were conducted with the base of the rubber nose removed. As the base is adhered to the cone section by the curing urethane alone, pull out tests must be conducted to prove that the base of the rubber nose can withstand forces it will encounter while in service. While the nose section of the rubber nose proved to be a very desirable option for use on SPAD, the base of the rubber nose must be analyzed to consider the rubber nose examined completely.

## **6.4 Foam Nose**

The Foam Nose was to be the simple solution. The elastomeric capabilities of foam were to create a solid structure that could collapse in on itself. The design was thoroughly analyzed in the bench-top environment and produced very undesirable results. It was found that the foam densities selected deformed greatly when small pressures were applied. This deformation is unacceptable while in flight. The foam noses also could not rebound to their original geometry after a 24 hold time. Because of this, the ability to rebound at all after a 5 year hold period was called into question. Since the foam nose cannot hold the required geometry, pack within the proper dimensions or rebound fully after compression it is recommended that the foam nose not be employed as a design solution for the SPAD nose.

## **6.5 Conclusion**

The data acquired in the analyses of each nose cone concept clearly presents definite rejections and possible candidates for application as the SPAD nose cone. The Inflatable Nose and the Foam Nose are the two designs concepts in which enough cause was found to not pursue as viable options. Since the volume of the pressure bottle was very quickly found to be in great excess of the requirements, for time management purposes the inflatable nose analysis ended. For that reason, no further analysis took place and recommendation cannot be given to use a system which has not been tested in full. The Foam Nose however, was exhaustively tested. The compression set results and the force to compress results show that this design could not successfully be used as the SPAD nose as the rebound time is too long and the rebound geometry does not match the design geometry. The Sping-Loaded Nose would be a very desirable option as it fits all of the required design criteria. However, due to its multiple parts the cost of production of each of the components must be reduced in order to make it the best design option.

The design concept which best conforms to the design requirements is the rubber nose. Its simplistic design creates an inexpensive component for SPAD that data shows can resist the pressure of flight and still compress for storage. It is because of the above conclusions that the Rubber Nose is recommended for further development as the SPAD nose cone.

---

## Acronyms

---

SPAD – Sonobuoy Precision Aerial Delivery

ADV – Air Delivery Vehicle

ASW – Anti-Submarine Warfare

SBIR – Small Business Innovation Research

R&D – Research and Development

SBA – Small Business Administration

RADAR – RADio Detection and Ranging

SONAR – SOund Navigation and Ranging

SLT – Sonobuoy Launch Tube

CONOPS – Concept of Operations

MPH – Miles per Hour

CFD – Computational Fluid Dynamics

FEA – Finite Element Analysis

KCI – KaZaK Composites, Incorporated

GPS – Global Positioning System

PSI – Pounds per Square-Inch

CAE – Computer Aided Engineering

---

## Appendix

---

### Navier-Stokes Equations (Anderson 2007)

$$\frac{\partial u}{\partial t} = -u \frac{\partial u}{\partial x} - v \frac{\partial u}{\partial y} - w \frac{\partial u}{\partial z} + \frac{1}{\rho} \left[ -\frac{\partial p}{\partial x} + \frac{\partial \tau_{xx}}{\partial x} + \frac{\partial \tau_{yx}}{\partial y} + \frac{\partial \tau_{zx}}{\partial z} \right]$$

*Momentum in the x-Direction*

$$\frac{\partial v}{\partial t} = -u \frac{\partial v}{\partial x} - v \frac{\partial v}{\partial y} - w \frac{\partial v}{\partial z} + \frac{1}{\rho} \left[ -\frac{\partial p}{\partial y} + \frac{\partial \tau_{xy}}{\partial x} + \frac{\partial \tau_{yy}}{\partial y} + \frac{\partial \tau_{zy}}{\partial z} \right]$$

*Momentum in the y-Direction*

$$\frac{\partial w}{\partial t} = -u \frac{\partial w}{\partial x} - v \frac{\partial w}{\partial y} - w \frac{\partial w}{\partial z} + \frac{1}{\rho} \left[ -\frac{\partial p}{\partial z} + \frac{\partial \tau_{xz}}{\partial x} + \frac{\partial \tau_{yz}}{\partial y} + \frac{\partial \tau_{zz}}{\partial z} \right]$$

*Momentum in the z-Direction*



## Shear Stress Equations for Fluid Flow (Anderson 2007)

$$\tau_{xy} = \tau_{yx} = \mu \left( \frac{\partial v}{\partial x} + \frac{\partial u}{\partial y} \right)$$

$$\tau_{yz} = \tau_{zy} = \mu \left( \frac{\partial w}{\partial y} + \frac{\partial v}{\partial z} \right)$$

$$\tau_{zx} = \tau_{xz} = \mu \left( \frac{\partial u}{\partial z} + \frac{\partial w}{\partial x} \right)$$

$$\tau_{xx} = \lambda (\nabla \cdot \mathbf{V}) + 2\mu \frac{\partial u}{\partial x}$$

$$\tau_{yy} = \lambda (\nabla \cdot \mathbf{V}) + 2\mu \frac{\partial v}{\partial y}$$

$$\tau_{zz} = \lambda (\nabla \cdot \mathbf{V}) + 2\mu \frac{\partial w}{\partial z}$$

---

## References

---

Anderson Jr., John D. (2007). *Fundamentals of Aerodynamics*. (4<sup>th</sup> ed.). New York: McGraw Hill.

ANSYS, Inc. (2006). *ANSYS Mechanical* (Release 11.0) [Computer Software]. Canonsburg, PA: ANSYS, Inc..

Harkness Industries, Inc. (2006). *Urethane Products Selector Guide*. Retrieved July 22, 2008, from: [http://www.harknessindustries.com/pdfs/Product\\_Guide.pdf](http://www.harknessindustries.com/pdfs/Product_Guide.pdf)

Hibbeler, R.C. (2008). *Mechanics of Materials* (7<sup>th</sup> ed.). Upper Saddle River: Pearson Prentice Hall.

Oberg, Erik, F. D. Jones, & H.L. Horton (Eds.). (2000). *Machinery's Handbook* (26<sup>th</sup> ed.). New York, NY: Industrial Press Incorporated.

OPNAV (September 1998). *Approved Navy Training System Plan for the Navy Consolidated Sonobuoys* (N88-NTSP-A-50-8910B/A). United States: U.S. Government Printing Office.

Pope, Alan. (1966). *Wind-Tunnel Testing* (2<sup>nd</sup> ed.). United States of America: John Wiley & Sons, Inc.

Raymer, Daniel P. (2006). *Aircraft Design: a Conceptual Approach* (4<sup>th</sup> ed.). Reston: American Institute of Aeronautics and Astronautics, Inc.

Reynolds Advanced Materials. (2008). *Everything You Need for Mold Making & Casting*.

Schlichting, Dr. Hermann. (1968). *Boundary-Layer Theory* (6<sup>th</sup> ed.). United States of America: McGraw Hill.

United States Office of the Joint Chiefs of Staff (2001). *Joint Doctrine for Amphibious Operations* (JP-3-02). United States Navy.